



Contents lists available at ScienceDirect

Journal of Marine Systems

journal homepage: www.elsevier.com/locate/jmarsys

Q1 1 Interannual-to-interdecadal variability of the Yellow Sea Cold Water Mass in 2 1967–2008: Characteristics and seasonal forcings

3 Sunghyea Park ^{a,*}, Peter C. Chu ^a, Jae-Hak Lee ^b

4 ^a Department of Oceanography, Naval Postgraduate School, Monterey, CA, USA

5 ^b Marine Environment and Climate Change Laboratory, Korea Ocean Research & Development Institute, Ansan, Republic of Korea

ARTICLE INFO

Article history:

8 Received 18 June 2010

9 Received in revised form 15 March 2011

10 Accepted 24 March 2011

11 Available online xxxx

Keywords:

14 Yellow Sea Cold Water Mass

15 Interannual-to-interdecadal variability

16 Seasonal forcings

A B S T R A C T

We identified characteristics of interannual-to-interdecadal variability of the Yellow Sea Cold Water Mass and examined mechanisms to generate variability using the Korea Oceanographic Data Center dataset. Regional/background variables (sea level pressure (SLP), surface air temperature (SAT), and sea surface temperature (SST)) and five climate indices were used to explore the linkage to seasonally-differential forcings. The first EOF mode (53%) represents warming/cooling over the entire bottom cold water with the dominant periods of 2–7 and 10–20 years. Three cold and two warm events occur in 1967–2008. The variability preliminarily attributes to previous winter surface forcings; however, summer surface forcings intensify bottom cold water temperature anomaly (BWTa) induced in the previous winter and also trigger a new anomaly, especially in the cold event after 1996. Cold events relate to the winter forcing (strengthening of the Siberian High, the Aleutian Low, East Asian Jet Stream, Pacific Decadal Oscillation, and Arctic Oscillation) and the summer forcing (increased SLP in the Asian continent and the Aleutian Islands and increased SST in the Kuroshio and the Alaskan Current). In both seasons, SST and SAT anomalies on the tropical to subtropical western North Pacific are strongly correlated to BWTa; however, mechanisms are different.

© 2011 Published by Elsevier B.V.

1. Introduction

The Yellow Sea (YS; also known as the Huanghai Sea) is a semi-enclosed marginal sea of the western North Pacific bordering the Korean Peninsula to the east and the Chinese mainland to the west, and the Bohai Bay to the north (Fig. 1). It is open to the East China Sea to the south, containing a well-developed shallow continental shelf. Many rivers drain into the YS, providing a huge quantity of sediments. In addition, high primary productivity of the sea water, a prevailing monsoon regime, abundant species in marine and coastal habitats, and approximately 600 million people around the YS demonstrate a wide diversity of the YS in perspectives of geography, biological environment, and socio-economics (Teng et al., 2005). These diverse characteristics have been drawing attentions from many academic and industrial sectors and drive us to focus on any changes in the YS related to a recent climate change.

The YS waters show marked seasonal variations owing to the shallow depth (average of 44 m) and the monsoon. However, the water in the central trough of the YS (Yellow Sea trough) displays less seasonality. In spring increased solar radiation heats the YS, but the water in the central trough, which is a remnant of cold, vertically well-mixed water in the previous winter, remains cold because of the depth.

* Corresponding author at: Department of Oceanography, Naval Postgraduate School, Monterey, CA93943, USA. Tel.: +1 831 656 7819; fax: +1 831 656 3686.
E-mail address: spark@nps.edu (S. Park).

As temperature gradient around the water becomes greater in spring through summer, the water is distinctively seen as a dome on the trough. The strong temperature gradient prevents the heat transfer from the surrounding so that the water can remain cold until breaking down in early winter (November). This cold water, because it is more noticeable in the temperature field, is called the Yellow Sea Cold Water Mass (YSCWM) in many literatures, also known as the Yellow Sea Bottom Cold Water. (Chu et al., 1997a, 1997b, 2005; Hur et al., 1999; Lie, 1986; Su and Weng, 1994; Zhang et al., 2008). It occupies ~30% of the total volume of the YS (Su and Weng, 1994). Since YSCWM is the most conservative among water masses in the YS, it is likely to contain clearer long-term signals than any other water masses in the YS. The long-term signals are essential to understand climatological evolutions of the YS.

In addition to the suitability of YSCWM for exploring the long-term variations of the YS, the year-to-year variation of YSCWM influences catches and fishing grounds of demersal fishes (Cho, 1982). YSCWM serves as an overwintering site for many temperate species (Wang et al., 2003; Wang and Zuo, 2004). The intensity of summer southward/southeastward-migration of YSCWM including the cold water over the eastern Yangtze Bank affects the upstream path of the Tsushima Warm Current, and eventually induces changes in the regional hydrography in the southern YS and the northern East China Sea (Park and Chu, 2006b). For these reasons, the study on the long-term variations of YSCWM would be informative to interpret variations in the related fields.

Earlier studies explored the relation of YSCWM to winter sea surface temperature or heat flux using observations for 10 to 20 years

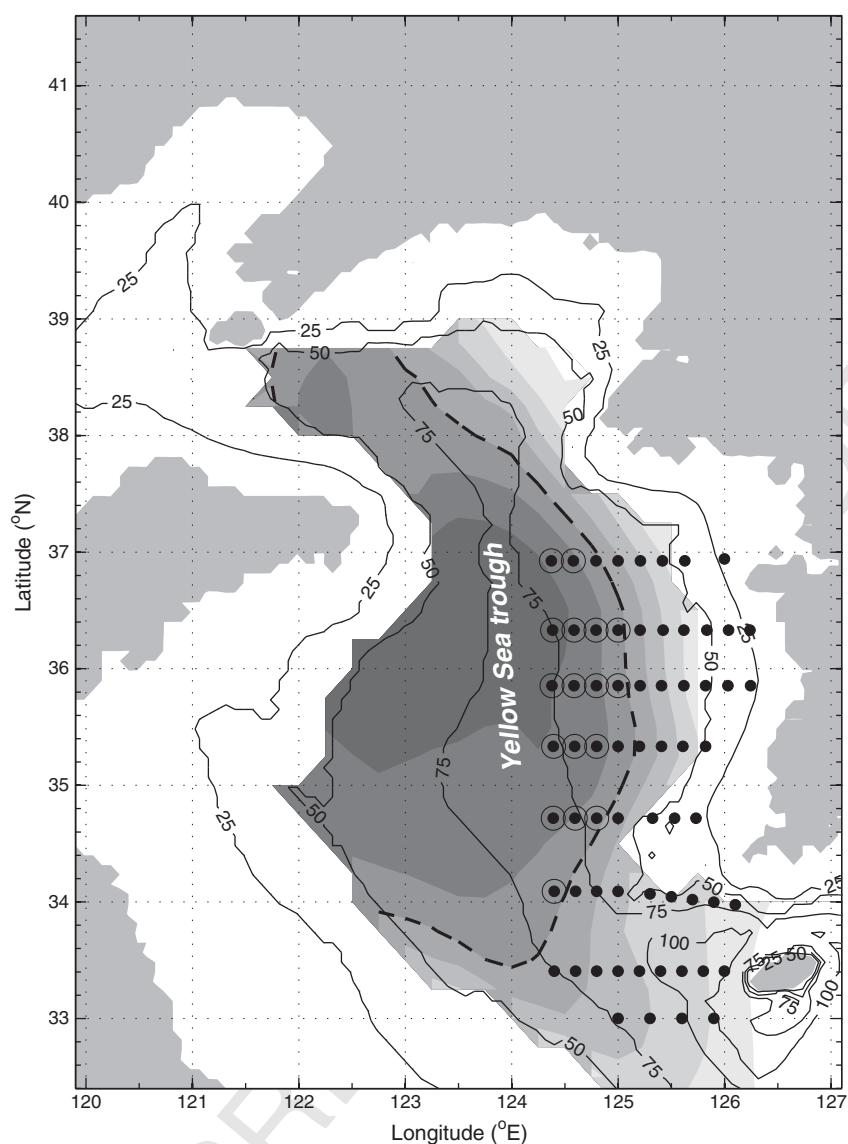


Fig. 1. Geography of the study area. Contours (m) indicate bottom topography. Shaded area with a shading interval 1 °C presents climatological August temperature distribution at 50 m depth from the Generalized Digital Environmental Model dataset: cooler temperature is darker, and an isotherm 11 °C is denoted by a dashed line. KODC data stations are denoted by black dots: large open circles indicate the stations where 42-year averaged August temperature at 50 m depth is colder than 11 °C.

(Han and Chang, 1978; Kang and Kim, 1987; Yang et al., 1984). Year-to-year variation of YSCWM was seen in those studies but was not discussed. Recently, Bai et al. (2004) reported that the position and the intensity of a thermocline dome over YSCWM vary interannually using data along 36°N section (120.5–124.5°E) from 1977 to 2003. In most El Niño years the thermocline dome shifts eastward and the top of the dome is at shallower depth, but temperature itself of YSCWM is not related to El Niño. Hu and Wang (2004) conducted EOF analysis on August temperature data along 34°N and 36°N sections from 1975 to 2003 and described variability at a thermocline depth (~20 m): in the vertical temperature section, temporal variance of temperature is greatest at the thermocline depth. Two time-series of the first mode principal component from 34°N and 36°N sections are quite different, although two sections reveal YSCWM obviously. It would be proper to apply EOF analysis to a horizontal temperature section at a specific depth where YSCWM is found climatologically. No studies have attempted to describe the long-term variation of YSCWM in a three-dimensional view.

As for what causes the long-term temperature variations of YSCWM, an atmosphere and ocean condition in the previous winter

has been known as a key factor, because once the winter condition 105 was imprinted on the water through air-sea interactions the water 106 would be secured in the bottom (Han and Chang, 1978; Kang and 107 Kim, 1987; Yang et al., 1984). If so, is there any other seasonal forcing 108 affecting YSCWM afterwards? YSCWM varies seasonally, despite 109 weak seasonality in comparison with the other water masses in the 110 YS: it becomes warm since May (Hur et al., 1999; Park and Chu, 111 2006b; Zhang et al., 2008). The shallow depth of the YS facilitates that 112 downward/positive heat flux during warm seasons transfers to the 113 bottom cold water against the thermocline. The bottom cold water 114 can contact with warmer water by a strong tidal mixing, which occurs 115 over the flanks of the YS trough, especially in summer (Lee and 116 Beardsley, 1999; Lie, 1989). However, the atmosphere and ocean 117 condition in warm seasons has been hardly addressed in studies of the 118 long-term variations of YSCWM. In addition, the connection of the 119 YSCWM variation with the atmosphere and ocean conditions in 120 remote regions should be investigated because the long-term 121 variation is remotely linked in larger, even global scales. 122

This study intends to identify characteristics of long-term variability 123 of YSCWM and to examine causes of the variability focusing on 124

125 seasonally differential forcings. In Section 2, we describe various
 126 datasets used for the study, i.e., the YSCWM temperature data,
 127 background atmospheric and oceanic data for the wider region, and
 128 climate indices. In Section 3, we conduct preliminary exploration of the
 129 YSCWM variability in the three-dimensional view. Then, we apply the
 130 empirical orthogonal functions (EOF) analysis on the temperature
 131 anomaly of the bottom cold water and examine how the anomalies
 132 evolve and where they are placed during cold/warm events. In Section 4,
 133 we examine the relationship between the summer surface temperature
 134 anomaly and the bottom temperature anomaly. In Section 5, we analyze
 135 the linkages between the bottom cold water variability and the remote
 136 summer/winter atmospheric and oceanic variables using the singular
 137 value decomposition (SVD) methods. We also discuss the lagged
 138 correlations with the climate indices.

139 2. Data

140 2.1. KODC data

141 There is no dataset which is eligible to cover the entire YSCWM as
 142 well as to display its long-term variations, as far as we are attainable.
 143 Fortunately, datasets are available south of 37°N, where the over 80% of
 144 the total volume of YSCWM exists (Su and Weng, 1994). In the area
 145 south of 37°N, the western side of 124.5°E was observed by China (for
 146 the location see (Bai et al., 2004, Fig. 1)) and the eastern by Korea (Fig. 1).
 147 Two datasets were collected independently and their station spacing
 148 and temporal coverage were different. The Korea dataset is a subset of
 149 the Korea Oceanographic Data Center (KODC) dataset (available at
 150 <http://www.nfrdi.re.kr>). The KODC dataset is a bimonthly (February
 151 through December) collection observed by the National Fisheries
 152 Research & Development Institute (Korea) since 1960. It contains
 153 oceanographic parameters of temperature, salinity, oxygen, phosphate,
 154 nitrite, and silicate at 175 stations around the Korea peninsula, i.e. the
 155 Yellow, South, and East/Japan Seas. Some parameters were not observed
 156 in certain periods, and temperature samples were least missed.

157 Sixty five stations are included in our study area (Fig. 1), covering
 158 the eastern part of YSCWM and the west coast of Korea. The Yellow
 159 Sea Warm Current region is unfortunately not covered, which might
 160 be associated with YSCWM in the winter. Horizontal spacing of the
 161 stations is ~0.2° in zonal and ~0.6° in meridional. The data were
 162 collected at the depths of 0, 10, 25, and 50 m in the early 1960s, but at
 163 the depths of 0, 10, 20, 30, 50, 75, and 100 m in the rest of the period.
 164 Since there were a number of missed samples before 1967, which was
 165 hardly interpolated by any methods, we adopted the data since 1967,
 166 i.e. 42 years of 1967–2008.

167 For controlling quality of the data, we deleted samples exceeding
 168 three times of standard deviation in temporal and spatial fields: here,
 169 the temporal field consists of 42 samples (1967–2008) of each month
 170 at each station. Then, we interpolated missing samples by EOF filling
 171 method (for details, see Beckers and Rixen, 2003; Park and Chu,
 172 2006a). The data were interpolated vertically at two additional depths
 173 of 40 m and 60 m.

174 To check the compatibility, the KODC dataset is compared to the
 175 NOAA/NCDC extended reconstructed global sea surface temperature
 176 (SST) data based on COADS data (ERSST version 2; hereafter, called as
 177 global SST) since there are no observational subsurface temperature
 178 profiles from the NCD data covering the concurrent period. Eight grid
 179 points of the global SST fall in the study domain. Fig. 2a shows SST
 180 anomaly (SSTa) time-series of the KODC dataset at 125°E, 35.9°N and
 181 the global dataset at 124°E, 36.0°N (nearest to the KODC data
 182 location). The global SSTa varies at a smaller extent because of
 183 differences in observation methods and preprocesses between the
 184 two datasets, whereas the KODC SSTa shows larger variability: the
 185 KODC SST is ~1.5 °C higher (lower) in August (February and April)
 186 than the global SST (not shown). However, the similarity in the long-
 187 term variation trend between the two time-series is perceived by the

undulating peaks of them. This similarity is more evident in the time-
 188 series of spatially-averaged non-seasonal SSTa (Fig. 2b); in this study
 189 the non-seasonal time-series indicates the time-series of all month
 190 after deleting an annual cycle, i.e. seasonal cycle (see the definition in
 191 Section 3.1). Another global dataset, International Comprehensive
 192 Ocean–atmosphere Data Set (ICOADS), shows the similar features as
 193 well. Since the seasonal cycle was deleted, the range of the variability
 194 is almost the same, –1.2 °C to 1.4 °C, among the three time-series.
 195 Although the KODC time-series retains more short-term features, the
 196 three datasets are consistent in the long-term scales such as
 197 interannual to interdecadal scales with the correlation coefficient of
 198 0.8. Therefore, the KODC dataset agrees well with other global
 199 datasets in terms of the long-term variability. 200

201 2.2. Background datasets

In addition to earlier studies on the connection of YSCWM 202
 variability to the local winter atmospheric and oceanic conditions, 203
 we mentioned in Section 1 that the summer conditions might be 204
 involved and the long-term variation is likely to be linked remotely in 205
 the larger spatial scale. In the western Pacific marginal seas, the local 206
 atmospheric and oceanic processes in both seasons are linked to the 207
 surrounding (larger spatial scale) atmospheric and oceanic conditions 208
 (Hong et al., 2001; Lau et al., 2000; Minobe et al., 2004; Park and Oh, 209
 2000; Ponomarev et al., 1999). Accordingly, we explore how the 210
 YSCWM variability is associated with the surrounding atmospheric 211
 and oceanic conditions. Since these conditions are interrelated (Gong 212
 et al., 2001; Gong and Ho, 2003; Lin et al., 2002; Wang et al., 2000; Wu 213
 and Wang, 2002), we use data over a wide region (70°E–150°W, 214
 0–80°N), which is called a background region. Background datasets 215
 for the analysis are sea level pressure (SLP), surface air temperature 216
 (SAT), and SST during the common period (1967–2008). The SLP and 217
 SAT datasets with a resolution of 2.5° × 2.5° are the NCEP Reanalysis 218
 derived data from the web site <http://www.cdc.noaa.gov/>. The SST 219
 dataset with a resolution of 2.0° × 2.0° is the NOAA NCDC ERSST 220
 version 2 from the web site at <http://iridl.ldeo.columbia.edu>. 221

222 2.3. Climate indices

Climate index is a simple figure to represent the status and timing of 223
 climate factors, but combines many observations into a generalized 224
 description of the atmosphere or ocean. It is devised to characterize the 225
 factors which impact the global climate system. To examine what 226
 climate factors are associated with YSCWM variability, five climate 227
 indices which had been used in studies on regional climate including YS 228
 were selected: Arctic Oscillation Index (AOI; Thompson and Wallace 229
 (1998); available at <http://tao.atmos.washington.edu> or www.cpc.ncep.noaa.gov), North Pacific Index (NPI; Trenberth and Hurrell (1994); 231
 available at <http://www.cgd.ucar.edu/~jhurrell/np.html>), Western 232
 Pacific Pattern Index (WPPI; Barnston and Livezey (1987); available at 233
<http://ingrid.ldgo.columbia.edu>), Multivariate ENSO Index (MEI; Wolter 234
 and Timlin (1993, 1998); available at <http://www.cdc.noaa.gov>), and 235
 Pacific Decadal Oscillation Index (PDOI; Zhang et al. (1997), Mantua 236
 et al. (1997); available at <http://jisao.washington.edu/pdo>). AOI is 237
 characterized by SLP anomalies of one sign in the Arctic and opposite 238
 sign centered about 37–45°N. NPI is an area-weighted SLP over the 239
 region of 160°E–140°W and 30–65°N. It is a good index of the intensity 240
 of the Aleutian Low as well as an indicator of major climate processes in 241
 the North Pacific. WPPI represents a primary mode of low-frequency 242
 variability over the North Pacific for all months. MEI is an average of the 243
 main ENSO features contained in six observed variables over the tropical 244
 Pacific. A positive value of the MEI indicates the warm ENSO phase. 245
 PDOI, defined as the leading principal component of monthly sea surface 246
 temperature variability in the North Pacific (north of 20°N), is a long- 247
 lived El Niño-like pattern of the Pacific climate variability. 248

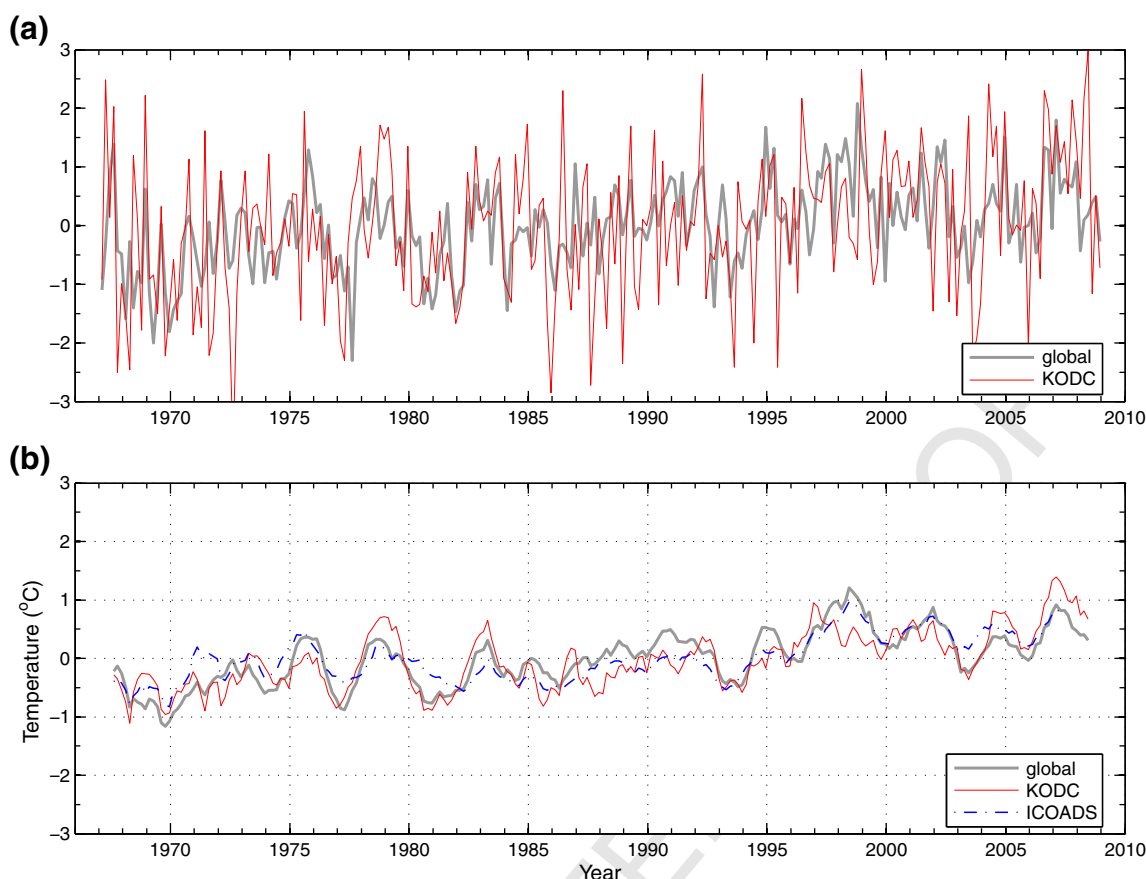


Fig. 2. SSTa time-series from KODC (125°E, 35.9°N), global (124°E, 36.0°N; nearest to the KODC data location), and ICOADS: (a) before removing the seasonal cycle (KODC and global), and (b) after removing the seasonal cycle (KODC, global, and ICOADS).

249 **3. Preliminary observations on YSCWM variability**

250 **3.1. Definitions of anomalies**

251 Let the sampling of a variable T be represented by $T(i, m, \text{and } y)$
 252 with $i (= 1, 2, \dots, I)$ for horizontal location, $m (= 1, 2, \dots, M)$ for month,
 253 and $y (= 1, 2, \dots, Y)$ for year. Here, $I=65$, $M=12$, and $Y=42$. The
 254 spatial average is given by

$$\bar{T}_i(m, y) = \frac{1}{I} \sum_i T(i, m, y), \quad (1)$$

256 and the yearly average is represented by

$$\bar{T}_y(i, m) = \frac{1}{Y} \sum_y T(i, m, y), \quad (2)$$

258 which is the seasonal variation at the location i . The temporal anomaly
 259 relative to the seasonal cycle at the location i is defined by

$$Ta(i, m, y) = T(i, m, y) - \bar{T}_y(i, m), \quad (3)$$

260 and its spatial (horizontal) average is

$$\bar{Ta}_i(m, y) = \frac{1}{I} \sum_i Ta(i, m, y). \quad (4)$$

263 The temporal anomaly $Ta(i, m, y)$ is reshaped into
 264

$$Ta(i, t) = Ta(i, m, y) \text{ for } t = (m, y), \quad (5)$$

and so is the spatial average,

266

$$\bar{Ta}_i(t) = \frac{1}{I} \sum_i Ta(i, t). \quad (6)$$

268

Time-series defined by Eqs. (5) and (6) is called “non-seasonal”
 269 time-series as it includes all months. In contrast, those defined by Eqs.
 270 (3) and (4) is called the time series for a certain month or season: for
 271 instance, “August” time-series or “summer” time-series.
 272

3.2. YSCWM variability in August

273

We assume temperature at 50 m depth as the characteristic field
 274 to represent the variability of YSCWM for the following reasons: 275
 (1) YSCWM is clearly seen in temperature field at 50 m depth 276
 regardless of the seasonal variation of YSCWM, (2) the KODC data 277
 were collected at the 50 m depth, and (3) temperature field at the 278
 50 m depth has been frequently seen in other studies of YSCWM 279
 (Isobe, 1999; Lie et al., 2000; Park, 1986; Zhang et al., 2008). The cold 280
 water covers the domain throughout all depth in February through 281
 April and still remains in the bottom in summer. In spatially-averaged 282
 time-series, the 50 m temperature defined by Eq. (1) increases after 283
 April, reaches highest in October, and then rapidly decreases from 284
 December to February (Fig. 3a). The variability of 50 m temperature 285
 anomaly defined by Eq. (4) is larger in August/October (-3.0 – 3.0 °C) 286
 than in February/April (-1.5 – 1.5 °C) (Fig. 3b). The larger temper- 287
 ature anomalies are also found in August at 60 m and 75 m depth (not 288
 shown) and at 50 m depth averaged over only the YS trough (open 289
 circle-marked stations in Fig. 1). At 50 m depth, the correlation 290
 coefficient is 0.86 between August and annual-mean temperature 291
 anomalies. In addition, YSCWM covers a great portion of August 292

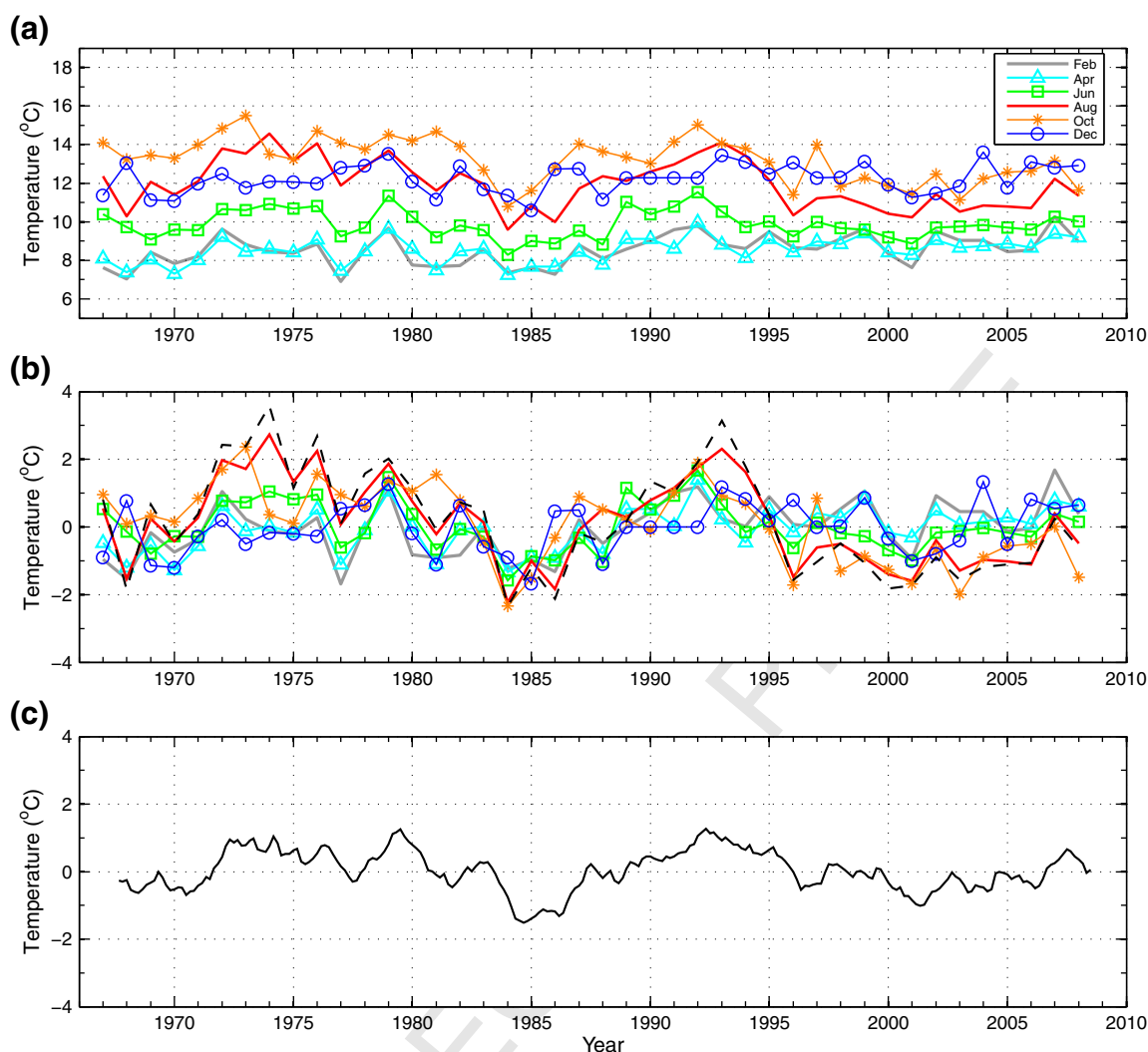


Fig. 3. (a) Bimonthly time-series of spatially-averaged temperature at 50 m depth. (b) Bimonthly time-series of spatially-averaged temperature anomaly at 50 m depth: another August 50 m temperature anomaly averaged over the open circle-marked stations in Fig. 1 is denoted by a dashed line. (c) Non-seasonal, i.e. after removing the seasonal cycle, time-series of spatially-averaged temperature anomaly at 50 m depth.

293 horizontal temperature field. Thus, the variability of August 50 m
 294 temperature/temperature anomaly is appropriate to represent the
 295 variability of YSCWM. Hereafter 50 m temperature/temperature
 296 anomaly is called bottom water temperature (BWT)/bottom water
 297 temperature anomaly (BWTa).

298 3.3. Conservativeness of YSCWM

299 The BWTa of each month varies similarly regardless of the month,
 300 although less similarity is shown in 1972–1976 and after 1996 than the
 301 other periods (Fig. 3b). The temporal variability pattern of August BWTa
 302 is similar to that of a non-seasonal time-series of 50 m temperature
 303 anomaly defined by Eq. (6) (hereafter referred as non-seasonal BWTa)
 304 (Fig. 3c) with a correlation coefficient of 0.83 between them. The
 305 similarity confirms conservativeness of YSCWM, which is also found in
 306 the correlation maps of August BWTa (spatially-averaged by Eq. (4)) to
 307 each month temperature anomaly (at each station by Eq. (2)): the
 308 correlation maps display correlation coefficients between them at 0, 10,
 309 20, and 50 m depths (Fig. 4). The coefficients greater (less) than or equal
 310 to 0.3 (–0.3) are contoured by white (black) solid lines. A correlation
 311 coefficient of >0.4 between August BWTa and temperature anomaly of
 312 the other months (denoted by white solid lines) lasts from February
 313 through October, especially at 30 m, 40 m, and 50 m (Fig. 4; 30 m and
 314 40 m distributions are not shown). No correlation is seen in December,

315 because YSCWM shrinks and might migrate out of the data domain
 316 during the fall transition of YS circulation and the beginning of winter
 317 monsoon (Lie et al., 2001; Naimie et al., 2001).

318 Taken a closer look, the temporal patterns of BWT and BWTa are
 319 identical in February and April, and then slightly different from June
 320 through October (Fig. 3a and b). BWT is most rapidly warmed from June
 321 to August. February/April BWTa shows a warming after 1996: this
 322 warming trend was observed in many regions associated with the recent
 323 global warming since the late 1990s (McPhaden, 2002; Minobe, 2002;
 324 Minobe et al., 2004; Oelke et al., 2004; Park and Chu, 2006a). In contrast,
 325 August/October BWTa shows cooling. These features imply that the
 326 variability of YSCWM can be regulated in summer after primarily driven
 327 by previous winter forcing. In addition, strong correlation at the surface
 328 (≤ 0.6) and 10 m depth (≤ 0.5) over the YS trough in June demonstrates
 329 a possibility of the summer regulation (denoted by white solid lines in
 330 Fig. 4), which will be examined in Section 4.2.

331 4. Characteristics of YSCWM variability

332 4.1. Spatiotemporal variability of YSCWM

333 We applied the EOF analysis on August BWTa, defined by Eq. (3), to
 334 identify the spatiotemporal variability of YSCWM. The first mode
 335 accounting for 53% of the August BWTa variability shows warming or

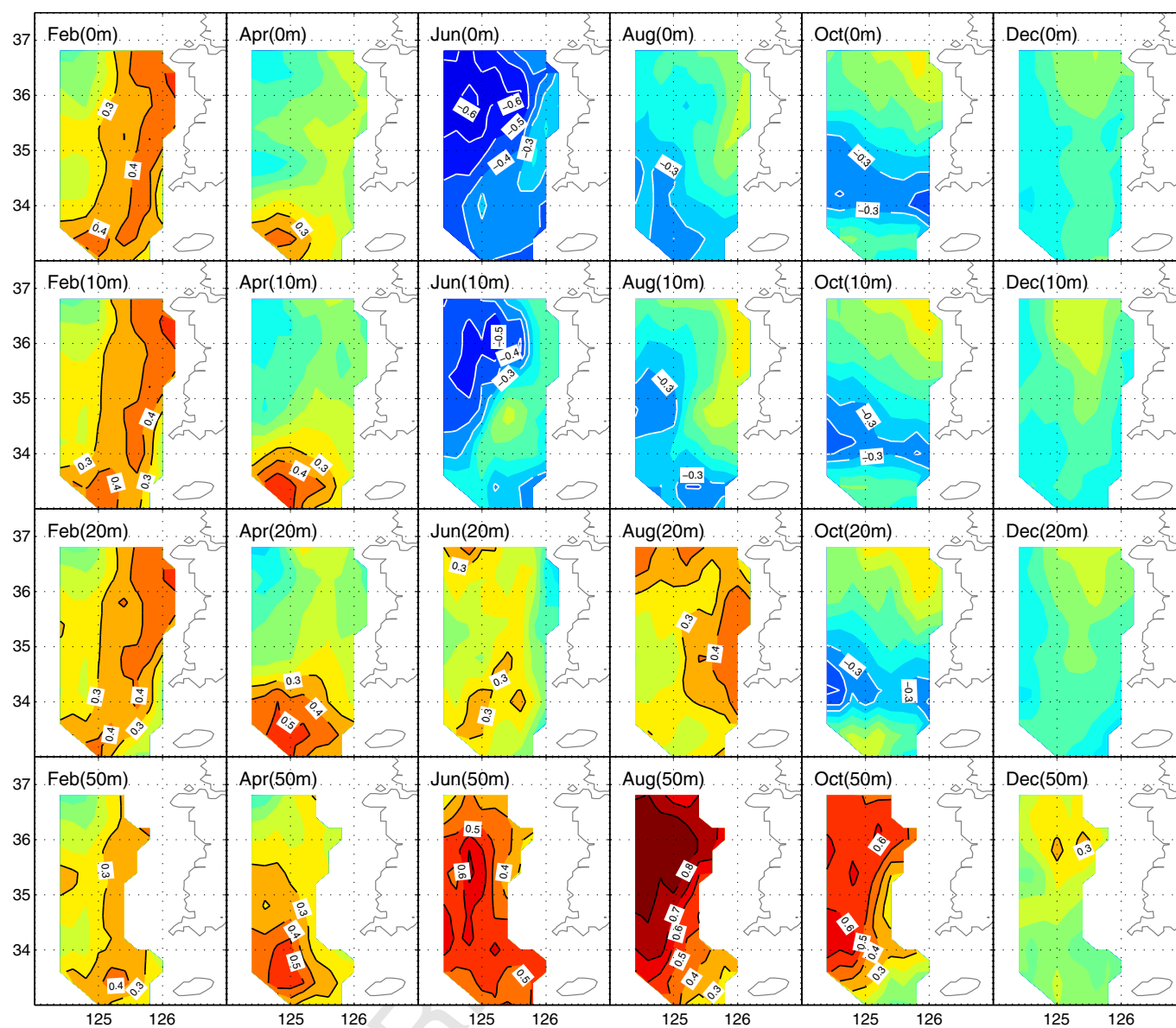


Fig. 4. Correlation coefficients between the spatially averaged BWTa for August and temperature anomaly for other months at each station at 0, 10, 20, and 50 m depths. The coefficients greater (less) than or equal to 0.3 (−0.3) are contoured by black (white) solid lines (contour interval 0.1).

cooling over the entire domain with highest amplitude in the YS trough, where YSCWM exist climatologically (Fig. 5a). A dominant period is identified as 2–7 years (interannual) and 10–20 years (decadal to interdecadal) by spectral analysis (Fig. 5b and c). Two and half (or two) decadal-to-interdecadal cycles are found in Fig. 5b. Two cold events ($\Delta T = -4^\circ\text{C}$) occur approximately in 1967–1971 and in 1983–1988 (Fig. 5d). Another cold event ($\sim -3^\circ\text{C}$) that begins in 1996 appears to last until the data are available or end up in 2005/2006: it is hard to determine at this moment. Two warm events last in the 1970s and the early 1990s.

The second mode (13%) presents a north–south dipole pattern (not shown). It varies in the interannual timescale but not in the decadal to interdecadal timescale. As the horizontal coverage of the KODC data is the eastern half of YSCWM, local detailed patterns in the data might be too small to be physically significant for the entire YSCWM. Accordingly, we do not discuss the second and higher modes. We focus the warming or cooling over the entire data domain. The EOF analysis of the non-seasonal BWTa produces the almost identical pattern with that of August BWTa (not shown). The cooling trend after 1996 is also clear in the non-seasonal EOF.

4.2. Distribution and evolution of anomalies during cold and warm events 356

4.2.1. Cold events 357

As the magnitude of the anomaly greater than 2°C is defined as an ‘event’, YSCWM reveals three cold events (1967–1971, 1983–1988 and 1996–2006) and two warm events (1972–1980 and 1990–1995), although the anomaly is little weak during 1990–1995 (Fig. 5d). Since the cold event of 1967–1971 is rather short and its beginning is uncertain because of the temporal coverage of the data, we used the last two of the three cold events to create composite maps of the events. The composite maps of spatial distributions of temperature and its anomalies for each event are plotted in Fig. 6. Vertical maps of June temperature anomaly are shown in Fig. 6c and d, as August BWTa shows the strong correlation with June temperature anomaly at the surface and 10 m depth (Fig. 4). Since cold anomaly cores are located little north than warm anomaly cores, a section along 35.3°N (34.7°N) is chosen for the cold (warm) events.

In the cold events, YSCWM is voluminous as well as colder, extending to the coast to cover the entire YS trough (Fig. 6a). As a result, the maximum anomaly ($\leq 2^\circ\text{C}$ in two cold events) is formed 374

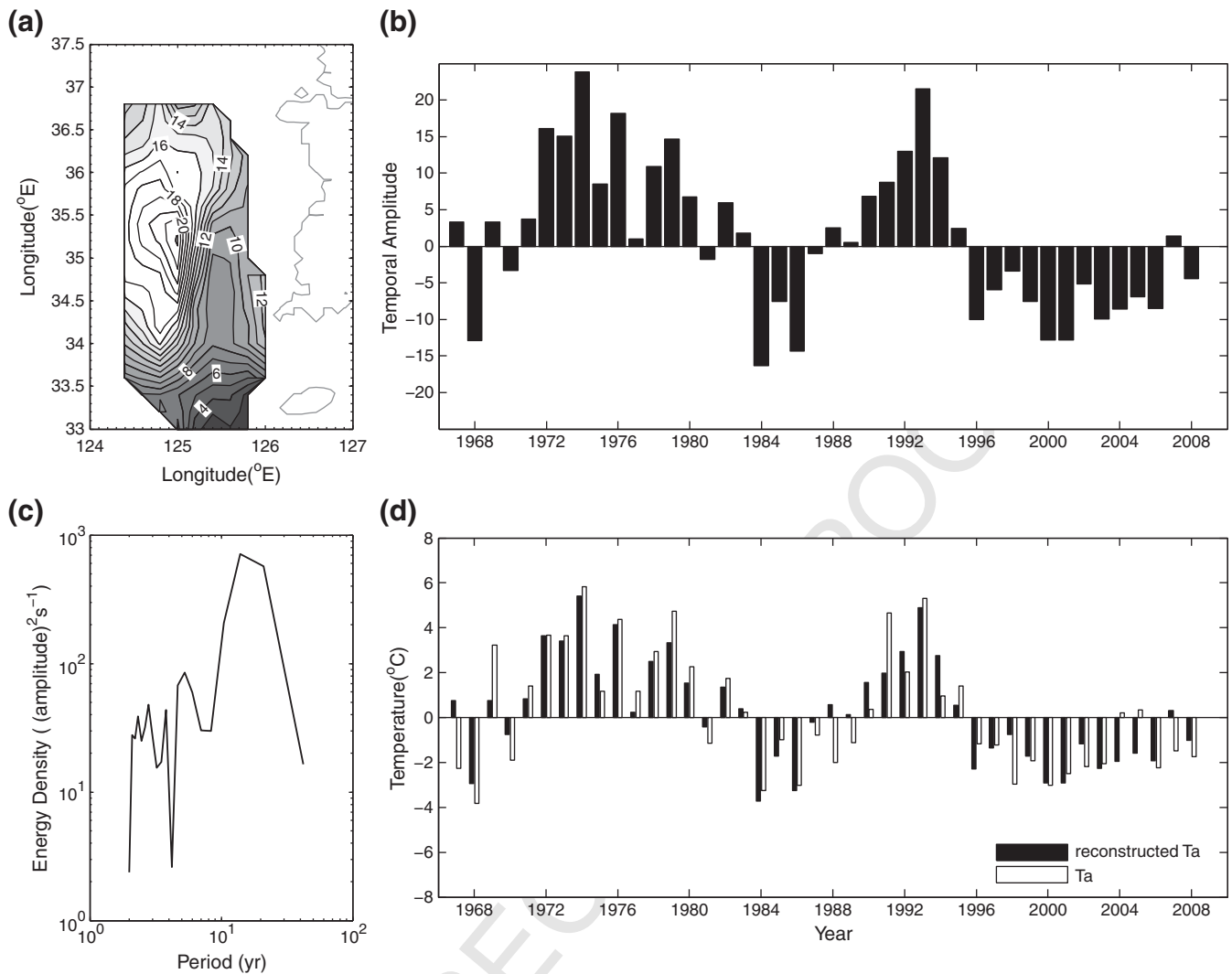


Fig. 5. The EOF analysis of August BWTa: (a) first EOF mode (unit 0.01 °C), (b) first principal component (non-dimensional), (c) spectrum of the first principal component, and (d) BWTa (white bars) and reconstructed BWTa (black bars) using the first EOF mode at the location with the maximum spatial amplitude. Note that BWTa is around 5.3 °C in 1974 (Fig. 5d), which is the multiplication of 0.21 °C (Fig. 5a) by 25 (Fig. 5b).

375 around the rim of YSCWM, where the horizontal temperature gradient
 376 is strong, rather than in the core of YSCWM. Note that a warm anomaly
 377 is shown in the upper layer in June during the two cold events; see
 378 opposite signs of anomaly between the upper and the lower layers
 379 (Fig. 6c). The same anomaly pattern is also seen in August. Such an
 380 anomaly pattern, the warmer upper layer and the colder lower layer,
 381 produces stronger vertical temperature gradient across the thermocline,
 382 in comparison with the normal year (non-event year).

383 A negative correlation is found between August BWT and June
 384 temperature difference at 10–40 m depths (Fig. 7). Here, we may
 385 assume that 10 m (40 m) depth is above (below) the thermocline.
 386 YSCWM is considerably warmed from June to August, as seen in
 387 Fig. 3a. The warming is proceeded mainly by downward heat transfer
 388 from the surface through the thermocline. In the cold events, as the
 389 intensified vertical temperature gradient of the thermocline impedes
 390 the downward heat transfer, the warming of YSCWM from June to
 391 August slows down compared to the normal year. Consequently,
 392 YSCWM is not warmed as much as in the normal year.

393 4.2.2. Warm events

394 In the warm events, a water mass with temperature less than 11 °C
 395 is hardly seen and the spatial-averaged temperature increases up to

15 °C (Figs. 3a and 6b). The water with temperature higher than 13 °C
 is spread from the coast to the south, and YSCWM is shrunk to the
 northwest (not shown). The maximum anomaly (>3 °C in two warm
 events) is formed south of the core of YSCWM. The signs of anomaly,
 colder upper layer and warm lower layer, is opposite to those in the
 cold events (Fig. 6d). Weaker vertical temperature gradient of the
 thermocline facilitates the downward heat transfer, and YSCWM is
 accordingly overheated compared to the normal year: August BWTa is
 warm when vertical temperature difference of June is small (Fig. 7).
 As closer to the coast, contour lines of the anomaly in the lower layer
 rises up and extends to the surface (Fig. 6d), probably due to strong
 summer turbulent mixing by the tide (Lee and Beardsley, 1999; Lie,
 1989). An evident positive correlation (>0.4) near the coast confirms
 this feature (Fig. 4–August 20 m), because less energy is needed to
 break weaker thermocline.

4.2.3. Time–depth diagram of anomalies

Provided that June temperature in the upper layer affects August
 BWTa, it is necessary to ascertain if the anomaly occurring in the
 previous winter is still retained in the bottom layer and to identify if the
 anomaly is transferred vertically. To do so, we plotted a time–depth

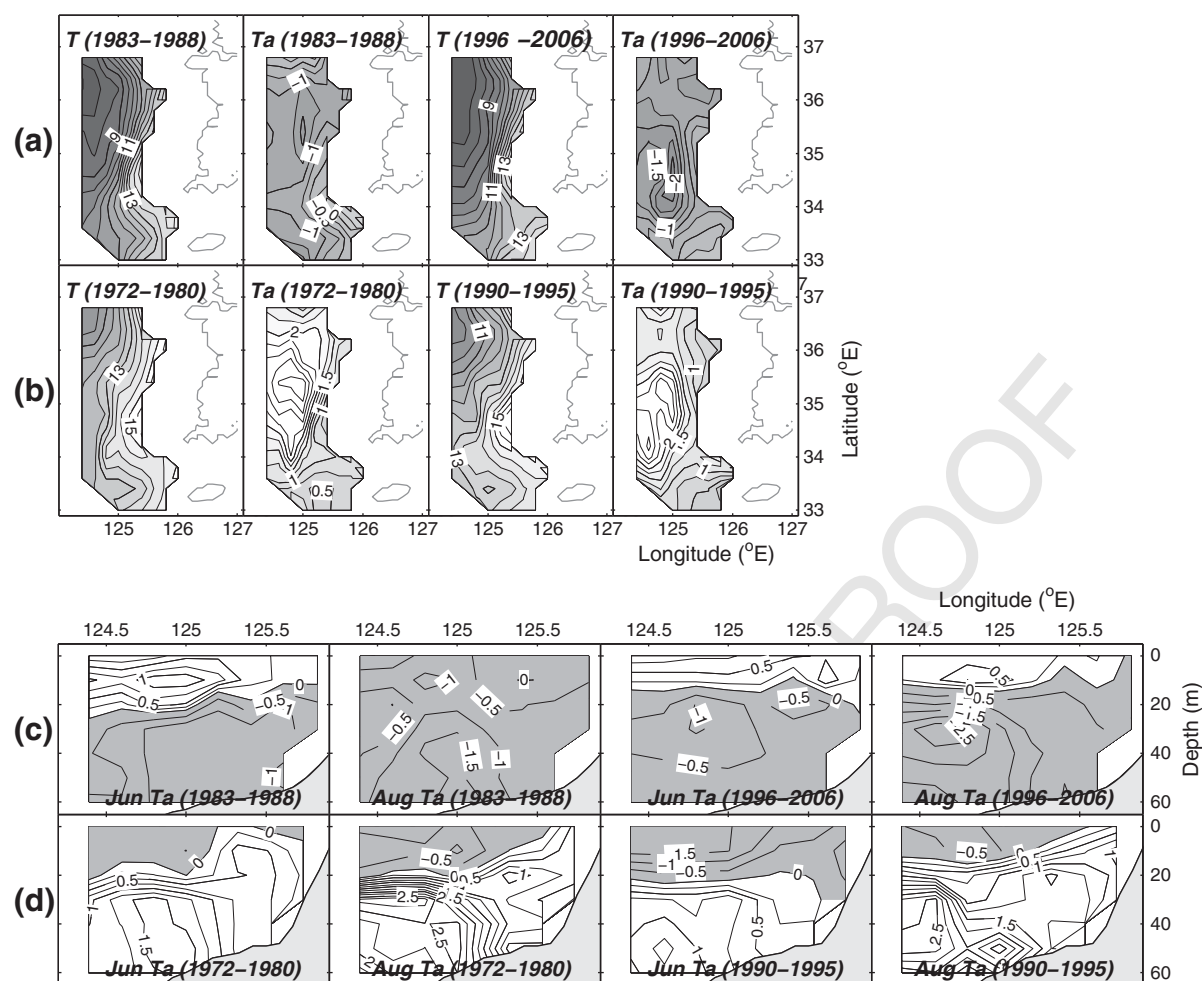


Fig. 6. Horizontal composite maps of temperature and temperature anomaly during cold events (a) and warm events (b): the maps show August distributions. Vertical composite maps of temperature anomaly during cold events (c) and warm events (d): the maps show June and August distributions. A section along 35.3°N (34.7°N) is chosen for cold (warm) events.

416 diagram of the temperature anomalies at the location with the
417 maximum amplitude of the first EOF mode (Fig. 8).

418 The anomaly in the bottom layer (assumed as deeper than 40 m) is
419 sustained throughout the events (see persistent warm (white)/cold
420 (gray) anomalies residing at deeper than 40 m in Fig. 8a–d), although
421 the anomaly strengthens in summer or disappears temporarily for
422 two or four months (see denser contours in summer and interruption
423 of the opposite anomaly at deeper than 40 m in Fig. 8a–d). The
424 temporal disappearance is probably due to the basin-wide seasonal

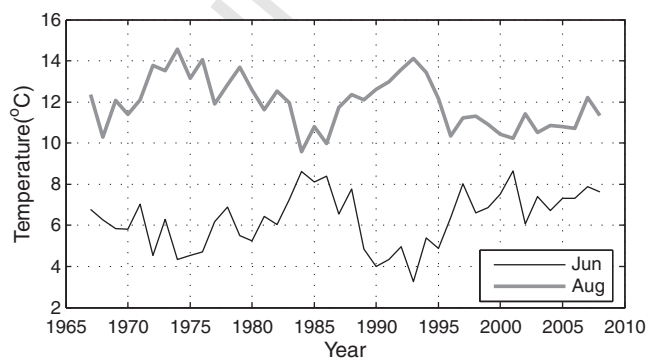


Fig. 7. Spatially-averaged August BWT and spatially-averaged June temperature difference between 10 m and 40 m depths.

425 circulation: in winter wind-driven southward flow is dominant along
426 the Korean and the Chinese coasts at surface, and northward flow near
427 bottom compensates the surface flow. In summer cyclonic circulation
428 is set up around YSCWM, and wind-driven northeastward flow is
429 dominant along the Chinese coast (Naimie et al., 2001).

430 During most of the events, the bottom layer has the same sign of
431 the anomaly as that of winter (December and February) surface
432 anomaly: for instance, the warm (cold) bottom anomaly in August
433 1973 (1984) and the warm surface anomaly in December 1972 (1983)
434 and February 1973 (1984). This feature evidences that the variability
435 of the bottom cold water attributes to that of the winter sea surface
436 as already known (Fig. 8a–c): the cold event after 1996 is an exception
437 (Fig. 8d). It is clearly seen that the anomaly with the opposite sign to
438 the bottom layer frequently develops in the upper layer in summer
439 and strengthens BWTa (for instance, the cold (warm) anomaly in
440 upper layer and the warm(cold) anomaly in the bottom layer in 1972
441 1983) summer are shown and their contours get denser.

442 Especially in the cold event after 1996, the winter anomaly forced
443 from the surface prevails throughout all the depth, but does not
444 sustain through summer (see that the warm February anomaly in the
445 upper layer does not reach to the bottom layer in August in Fig. 8d).
446 Instead the anomaly with the opposite sign to the winter surface
447 emerges in the bottom layer, develops over the event, and extends
448 upward (a summer cold anomaly is growing from the bottom layer in
449 1997–2004 in Fig. 8d). The summer cold anomaly matures most in
450 2004, then disappears temporarily, and emerges again in 2006. This

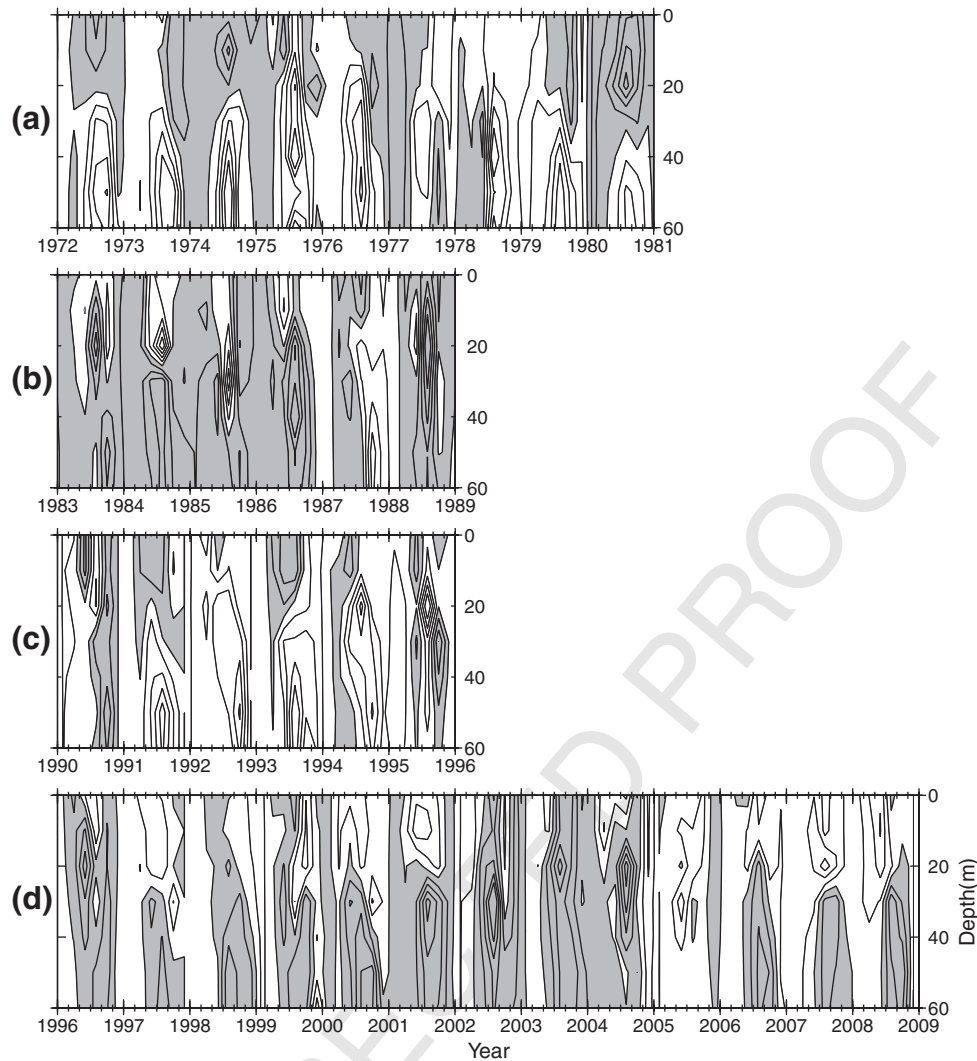


Fig. 8. A time–depth diagram of the temperature anomalies at the location with the maximum amplitude of the first EOF mode for two warm events ((a) and (c)) and two cold events ((b) and (d)). Cold anomalies are shaded. A contour interval is 1 °C.

451 cold anomaly emerges almost concurrently when the summer warm
 452 anomaly is turned on in the upper layer or right after then. From these
 453 features of anomaly evolutions, the summer surface forcing is capable
 454 of not only strengthening the bottom anomaly induced in winter but
 455 also triggering a new anomaly which is not originated from winter.

456 5. Relationship to background variables: seasonal forcings

457 5.1. Lagged correlation to climate indices

458 Correlation between principal component (PC) of each EOF mode
 459 and the climate indices reveals the relationship between YSCWM
 460 variability and climate factors. Since high correlation to a certain
 461 climate index implies that the corresponding climate factors are
 462 associated with YSCWM variability, the correlation would be a quick
 463 guidance to examine the relationship with the background variables.
 464 In addition, the correlation at a lagging/leading time reveals if two
 465 time-series are remotely related and which time-series leads.

466 In order to examine seasonal forcings of climate factors, winter
 467 (summer) climate indices averaged from December to February (June
 468 to August) are used. For instance, 1967 winter (summer) is an average
 469 of December 1967, January 1968, and February 1968 (June, July, and
 470 August 1967). Then, lagged correlation coefficients of PC of August
 471 BWTa to the five winter (summer) climate indices were calculated. A

negative lag indicates that the climate index leads the August BWTa 472
 (Fig. 9). The 95% confidence level for the correlation coefficients is 0.3. 473
 Only indices above the confidence level are displayed in Fig. 9. The 474
 correlation curves of the indices are different for the season. 475

5.1.1. Winter 476

The two indices (PDOI and NPI) are dominant in winter, in 477
 connection with the Aleutian Low. Negative PDOI and positive NPI 478
 indicate warming in the extratropical North Pacific. At zero lag August 479
 BWTa has highest correlation with PDOI (about -0.4) and NPI (about 480
 0.4) than any other indices (Fig. 9a). The BWTa also correlates with 481
 AOI (~ 0.3). However, February SSTa (or BWTa) shows rather higher 482
 correlation with AOI (~ 0.45) than the other climate indices (not 483
 shown); it is because there is a slight discrepancy between February 484
 SSTa and August BWTa in 1973–1976 and after 1996 (see February 485
 and August in Fig. 3b). At the sea surface the local winter climate of 486
 the YS seems to be more affected by AO, as seen in a good correlation 487
 of the first two modes of Japan/East Sea SSTa in interannual scales 488
 with AOI (Park and Chu, 2006a). 489

In addition to the concurrent correlation to PDOI and NPI, they lead 490
 the YSCWM variability by 2–3 years. The high correlation with zero, 491
 -2 year to -3 year lag could attribute to interannual undulations 492
 within the two indices time-series: PDOI reveals the tendency for 493
 year-to-year persistence along with positive or negative values 494

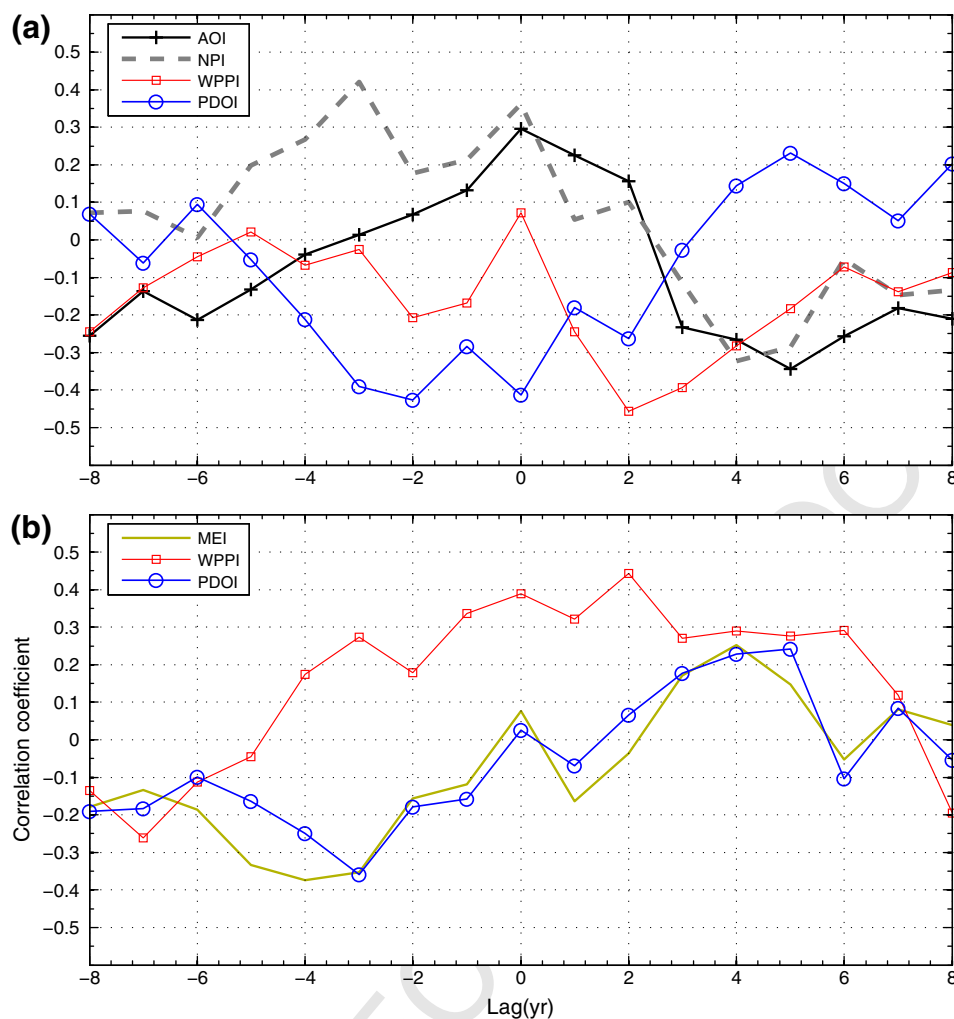


Fig. 9. Lagged correlation coefficients of the first EOF-PC of August BWTa with the five winter climate indices (a) and summer ones (b). A negative lag indicates that the climate index leads the August BWTa.

495 prevailing for 20–30 year periods (Zhang et al., 1997; Mantua et al.,
496 1997). Or it could attribute to remote propagation of PDO through
497 thermocline adjustment as detected in the Kuroshio extension (Deser
498 et al., 1999). Low correlation to MEI throughout the lags shows weak
499 linkage between winter ENSO links and BWTa (not shown).

5.1.2. Summer

500 The BWTa is correlated only with WPPI at 0–1-year lag (Fig. 9b).
501 Positive summer WPPI is related to cold SSTa in the tropical to
502 subtropical western North Pacific, indicating weak East Asian summer
503 monsoon (see maps at [http://www.cpc.ncep.noaa.gov/data/teledoc/
wp_map.shtml](http://www.cpc.ncep.noaa.gov/data/teledoc/wp_map.shtml)). Thus, the weak (strong) East Asian summer monsoon
504 is associated with the warm (cold) BWTa, followed by cool (warm) SSTa
505 over YS. According to negative correlation (about -0.35) with MEI
506 at -3 – 5 -year lag, a warm (cold) ENSO leads a cold (warm) BWTa by
507 3–5 years. Also seen in no correlation with MEI at zero lag, ENSO seems
508 to impact BWTa indirectly.
509
510

5.1.3. Climate indices for both winter and summer

511 In Fig. 9b the summer PDOI is correlated with BWTa at -3 -year lag
512 (about -0.4) as the winter PDOI, because the PDOI time-series of the
513 both seasons are congruent (correlation coefficient 0.6). The correla-
514 tion to PDOI is also seen in neighboring seas, such as the Japan/East
515 Sea (Gordon and Giulivi, 2004; Park and Chu, 2006a), the Bohai Sea
516 and the East China Sea (Han and Huang, 2008). WPPIs of the both
517 seasons display significant correlation coefficients at two-year lag,
518

and the correlation curves oscillate at periods of 2–3 years over the 519
lag. These correlation features of WPPI are accompanied by inherent 520
2–3-year variability in WPPI, based on a spectral analysis on WPPI 521
(not shown). As positive winter WPPI is related to warm SSTa in 522
the tropical to subtropical western North Pacific but cold SSTa in 523
the extratropical central North Pacific, the sign of the correlation 524
coefficient of the winter WPPI is opposite to that of the summer one. 525
The relation to SSTa in the tropical to subtropical western North 526
Pacific will be discussed further in Section 5.2.2. 527

5.2. Covariability with background variables

528 This section presents results of SVD analysis on covariability of the 529
August BWTa and winter/summer background variables (the temporal 530
mean for 42 years were deleted): SLP anomaly (SLPa), SAT anomaly 531
(SATa), and SST anomaly (SSTa). The winter (summer) data were 532
averaged in the same way as the climate indices. The SVD analysis is 533
the generalization of the EOF analysis. The EOF analysis is taken to 534
identify temporal and spatial variability of a single variable using the 535
autocorrelation matrix (a square matrix) (Björnsson and Venegas, 536
1997). The SVD analysis is taken to identify the covariance between 537
two variables using the covariance matrix (a rectangular matrix); for 538
instances, BWTa and winter SLPa in this study. Here, the temporal 539
patterns in the SVD analysis is also called PC. Normalized eigenvalues 540
explain a fraction of the covariance between the paired fields. 541
Heterogeneous correlation patterns, which are characteristic of SVD 542

Table 1
The first SVD mode of the background variables and August BWTa.

		Fraction of covariance (%)	Correlation coefficient of PCs	Fraction of BWTa variance (%)	Fraction of background variables' variance (%)
t1.4	Winter SLPa–BWTa	88	0.50	49	36
t1.5	Winter SATa–BWTa	78	0.61	51	16
t1.6	Winter SSTa–BWTa	78	0.69	51	14
t1.7	summer SLPa–BWTa	55	0.59	48	10
t1.8	summer SATa–BWTa	75	0.59	51	16
t1.9	summer SSTa–BWTa	78	0.55	50	19

analysis, are yielded by the correlation between PC time-series of one field and time-series of the other field at each of grid points. In other words, the patterns indicate how well BWTa at each grid point is predicted from the knowledge of PC of SLPa or vice versa.

Cherry (1996, 1997) offered caveats for SVD analysis and recommended first carrying out separate EOF analysis on the two data fields to check if the set of patterns is significantly correlated and physically meaningful. We carried out the EOF analysis on the winter/summer background variables and investigated if any leading (lower mode) PCs of the background variables show covariability with BWTa. In all cases BWTa showed the covariability with at least one of the three leading PCs of them. Therefore, the SVD results here are physically meaningful. We present only results of the first mode SVD for the same reasons we addressed in Section 4.1. The first mode SVD–BWTa resembles the first mode EOF–BWTa and accounts for a large fraction of BWTa variance, which is as good as the first mode of EOF–BWTa (the third column in Table 1). The results of SVD analysis are demonstrated as follows: for the example of a pair of SLPa and BWTa, a spatial pattern of SLPa/BWTa (Fig. 10a and d), a heterogeneous correlation pattern of BWTa/SLPa PC with SLPa/BWTa (Fig. 10b and e), and PC time-series of SLPa/BWTa normalized by its standard deviation (Fig. 10c).

5.2.1. Winter

5.2.1.1. SLPa. The first mode SVD–SLPa presents a dipole of the Siberian High and the Aleutian Low, a dominant winter atmospheric pressure distribution in the northern Hemisphere, and another high amplitude core in the Arctic (north of 70°N), which is the same sign as the Siberian High (Fig. 10a). This pattern resembles a composite of the first two EOF modes of winter SLPa (not shown). The heterogeneous correlation (correlation coefficient is 0.3 for 95% confidence level) is high in the dipole (≤ 0.6 in the Siberian High and > 0.4 in the western part of the Aleutian Low), indicating that cold event in YSCWM is associated with strengthening of both the Siberian High and the Aleutian Low (Fig. 10b). The relation to the Aleutian Low is confirmed by the significant correlation to NPI and PDOI. A negative correlation (≤ 0.3) in the Arctic is consistent with the correlation to AOI. Since AO affects the Siberian High and, in turns, the Siberian High does YSCWM, the correlation is lower in the Arctic than in the Siberian High.

The first mode SVD–BWTa (Fig. 10d) presents maximum amplitude in the YS trough, i.e. variability of YSCWM, which resembles the first EOF mode (see Fig. 5a). The heterogeneous correlation pattern

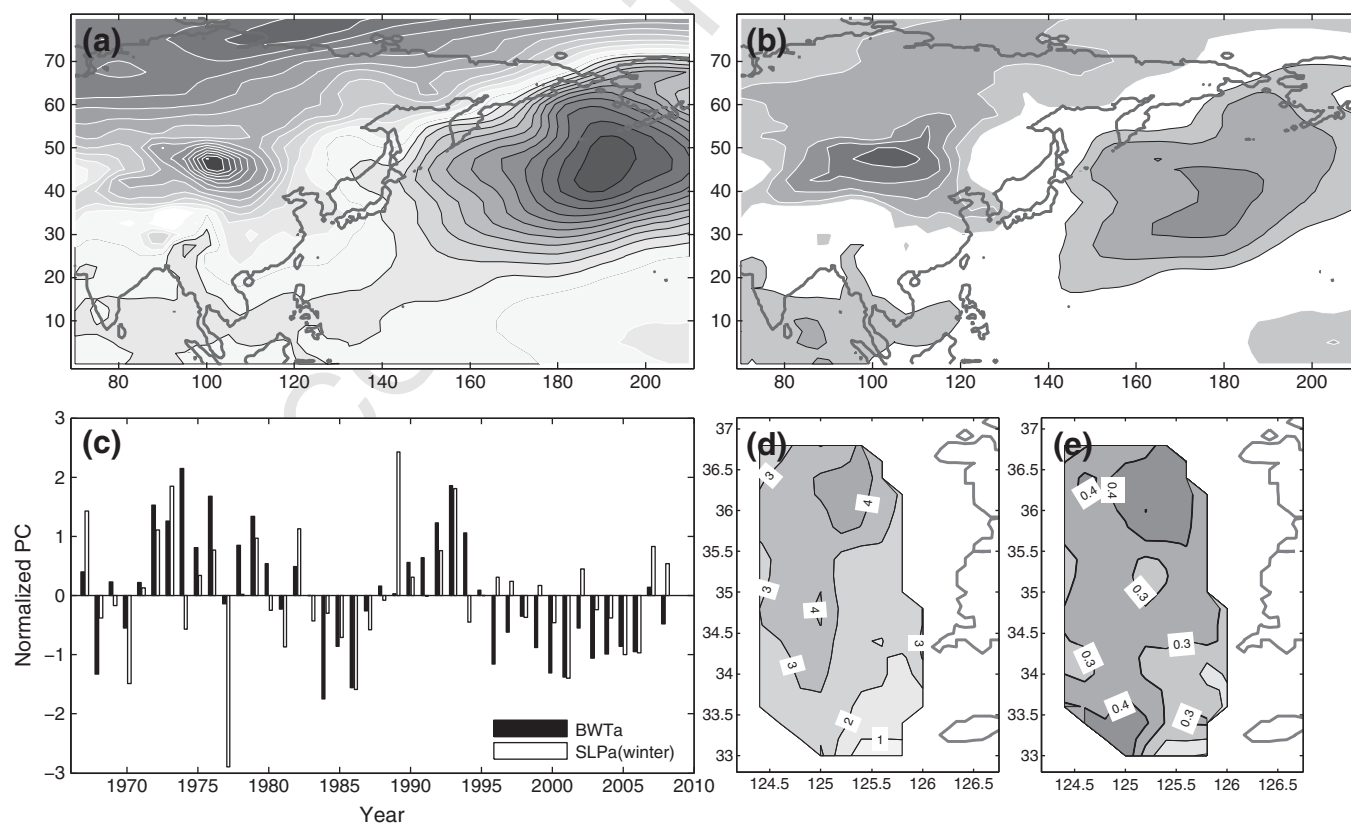


Fig. 10. The first SVD mode of winter SLPa–August BWTa: (a) spatial pattern of SVD–SLPa (negative (positive) white (black)-contoured; contour interval 1 hPa), (b) heterogeneous correlation coefficient pattern of SVD–SLPa (negative (positive) white (black)-contoured; contour interval 0.1; coefficient ≥ 0.2 is shaded), (c) temporal pattern of two SVD–PCs normalized by each PCs' standard deviation, (d) spatial pattern of SVD–BWTa (°C), and (e) heterogeneous correlation coefficient pattern of SVD–BWTa (figure configurations are same as (b)).

584 also resembles the first EOF mode, but the correlation is the highest in
 585 the northeastern part of the domain (Fig. 10e). The first mode
 586 accounts for 49% of BWTa variance, 36% of SLPa variance, and 88% of
 587 the covariance of the two fields (Table 1). Temporal variability of the
 588 first PC–BWTa mode in Fig. 10c is the almost same as that of EOF (see
 589 Fig. 5b). Two extreme variabilities are seen in the first PC–SLPa mode:
 590 strong low SLPa in 1977, which corresponds to the regime shift (1976/
 591 1977) in the North Pacific, and strong high SLPa in 1989, which
 592 corresponds to ENSO in 1988/1989. The winter SLPa and BWTa are
 593 correlated at 0.50.

594 5.2.1.2. SATa. The first SVD–SATa mode presents meridional variability of
 595 SATa, strong (weak) negative anomaly in the high (low) latitude and
 596 positive anomaly in the mid latitude (Fig. 11a). The first mode explains
 597 16% of variability of SATa, 78% of the covariance of the two fields
 598 (Table 1). The spatial pattern of SVD–SATa seems like a composite of the
 599 first and third EOF modes of winter SATa: (1) warming or cooling in
 600 northern Eurasian continent for the first EOF mode and (2) a meridional
 601 dipole north of 30°N and weak signal south of 30°N for the third EOF
 602 mode (not shown). BWTa is negatively correlated to SATa in the Arctic
 603 (≤ 0.5) and the tropical to subtropical western North Pacific (≤ 0.6),
 604 whereas positively to a zonal band covering 30–50°N (> 0.4) (Fig. 11b).
 605 This positive zonal band agrees with the position of the East Asian Jet
 606 Stream, a westerly with a maximum speed in the upper troposphere. The
 607 agreement implies the relation to the jet stream, because it affects the
 608 surface pressure system and winter air temperature field from
 609 the surface to the upper troposphere over East Asia and the western Pacific
 610 (Yang et al., 2002). With the comparison with the East Asian Jet Stream

index (see Yang et al. (2002, Fig. 3a)), PC–BWTa varies out of phase of
 611 East Asian Jet Stream index, i.e. colder BWTa when positive/stronger East
 612 Asian Jet Stream index. An interannual variability of neighboring sea, the
 613 Japan/East Sea SSTa, is also closely related with the jet stream (Park and
 614 Chu, 2006a). Note that the correlation is highest in the tropical to
 615 subtropical western North Pacific (Fig. 11b), although amplitude is weak
 616 in the spatial pattern (Fig. 11a) because the higher heat capacity of
 617 the sea triggers less temperature variation than that of the land does.
 618 PC–SATa and PC–BWTa are correlated at 0.61 (Fig. 11c). The two PCs
 619 are in good agreement in the 1970s and the 2000s, but rather poor
 620 agreement in the 1980s and the 1990s. Both the spatial pattern and
 621 the correlation pattern of SVD–BWTa resemble the first mode EOF,
 622 and the correlation is highest in the northeastern part of the domain
 623 (Fig. 11d and e).

625 5.2.1.3. SSTa. SVD–SSTa shows stronger signals in the midlatitude
 626 rather than in the tropics, indicating non-ENSO mode (Fig. 12a): a
 627 signal in the central to eastern tropical Pacific is still weaker than in
 628 the midlatitude in the case of SVD application to the entire Pacific (not
 629 shown). Its positive core reveals the eastern part of the Polar Front, i.e.
 630 an extension of the Kuroshio and the Oyashio, and extends to the
 631 central North Pacific, while its negative core spreads from the
 632 subtropical western to the central North Pacific. The correlation is
 633 > 0.3 (≤ 0.5) in the positive (negative) core (Fig. 12b). The other
 634 negative signals distribute along the Okhotsk Sea, the Bering Sea, and
 635 the Gulf of Alaska. This spatial pattern reflects a relation to PDO, as
 636 shown in the correlation analysis: see spatial patterns of decadal-scale
 637 temperature changes in the North Pacific by Deser et al. (1996, 1999).

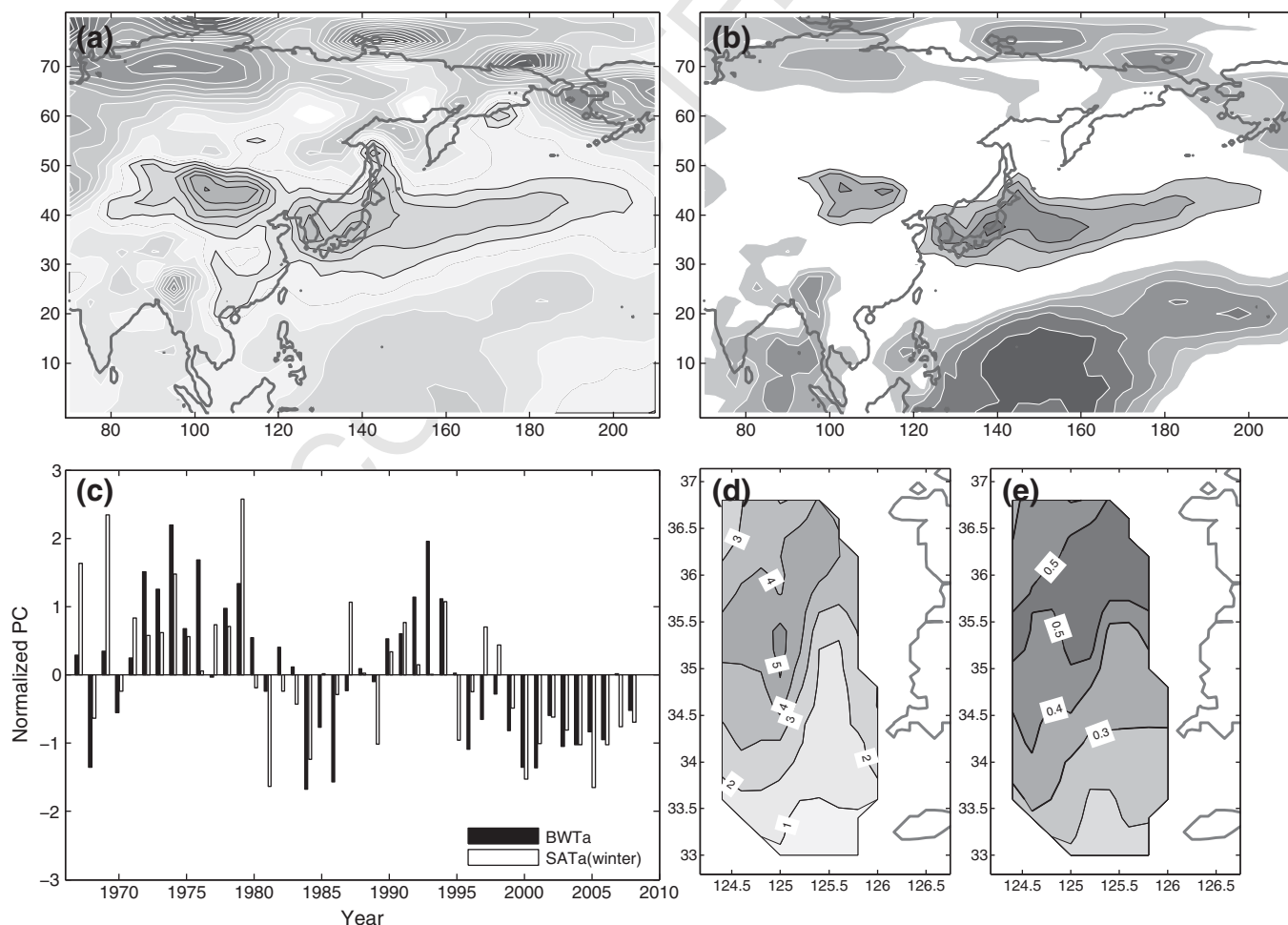


Fig. 11. The first SVD mode of winter SATa–August BWTa. Figure configurations are same as Fig. 10 except contour interval 0.5 °C in (a) and SVD–SATa.

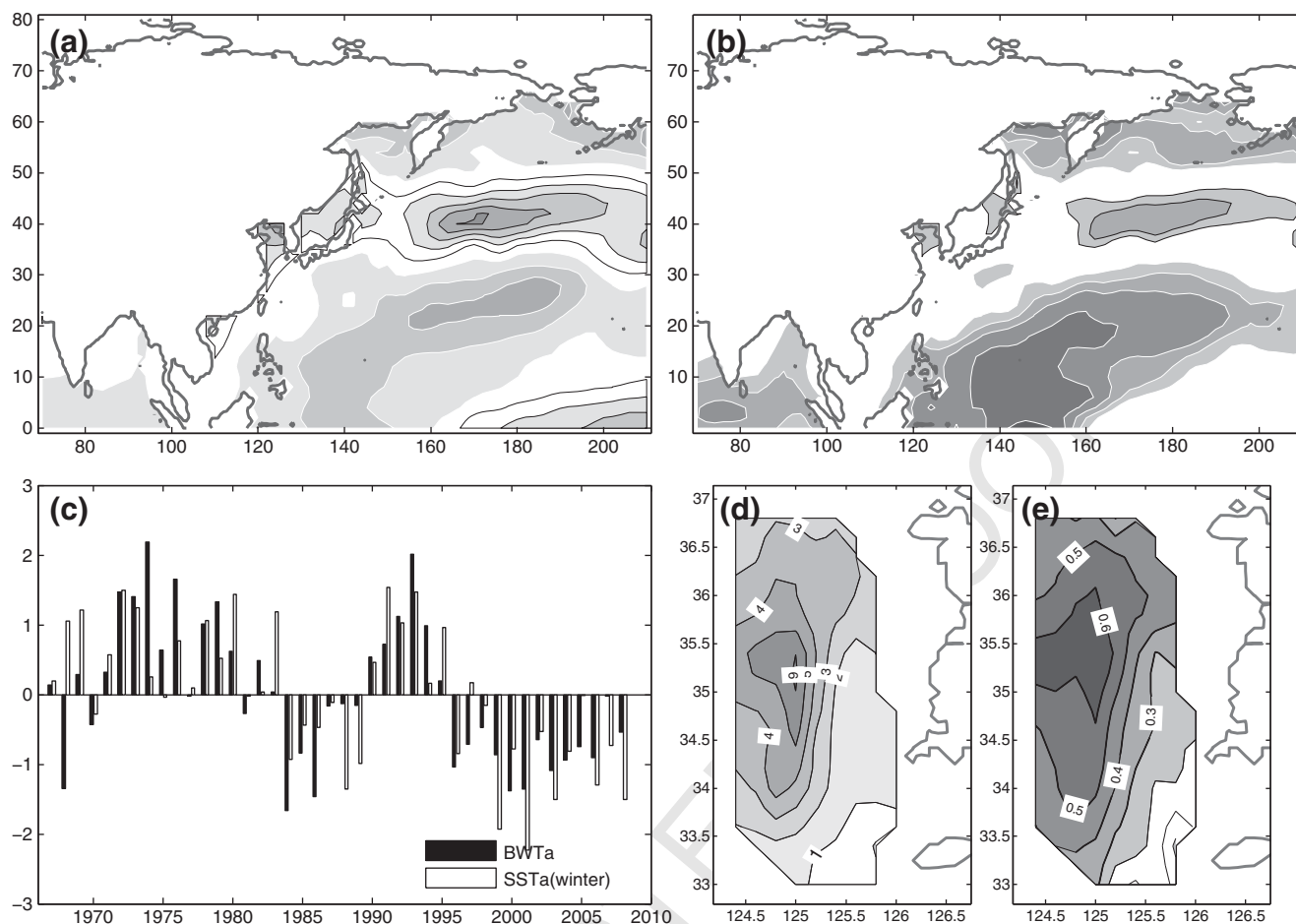


Fig. 12. The first SVD mode of winter SSTa–August BWTa. Figure configurations are same as Fig. 10 except contour interval 0.25 °C in (a) and SVP–SSTa.

638 Also the warm 1970s and the cold 1980s in the two PCs (Fig. 12c)
 639 coincide with PDO (Deser et al., 1996, 1999; Stephens et al., 2001).
 640 The 1976/1977 regime shift does not seem to impact the YS
 641 concurrently; first EOF–BWTa mode, although the maximum amplitude
 642 core is slightly shifted. Thus, we will explain the spatial patterns and
 643 the heterogeneous correlation patterns of the first SVD–BWTa mode
 644 without figures.
 645
 646
 647

648 5.2.2. Summer

649 In the following results, all of spatial patterns and heterogeneous
 650 correlation patterns of the first SVD–BWTa mode resemble the spatial
 651 pattern of the first EOF–BWTa mode, although the maximum amplitude
 652 core is slightly shifted. Thus, we will explain the spatial patterns and
 653 the heterogeneous correlation patterns of the first SVD–BWTa mode
 654 without figures.

655 5.2.2.1. SLPa. Summer SVD–SLPa shows two high amplitude cores on the
 656 Asian continent and the Aleutian Islands like the winter SVD–SLPa, but
 657 both cores show a same sign unlike the winter SVD–SLPa (Fig. 13a).
 658 The core on the Aleutian Islands is shifted northwestward and smaller than
 659 the winter SVD–SLPa, which is related with intensifying/expanding of
 660 the North Pacific High and weakening/retreating of the Aleutian Low
 661 in summer. The core on the Asian continent presents a low pressure
 662 formed by increased summer heating in deserts and dry land such as
 663 Gobi Desert. A positive core in the North Pacific, around 30°N, presents
 664 zonal migration/variation of the North Pacific High. A spatial correlation

665 pattern is similar to the spatial pattern of SVD–SLPa (Fig. 13b). The lower
 666 the pressure in the Asian continent and the Aleutian Islands is the
 667 warmer YSCWM is. The first mode explains 55% of the covariance of the
 668 two fields (Table 1), which is lower than the winter case. However, the
 669 correlation of the two PCs is stronger (0.59) than the winter case, due to
 670 greater similarity between the two PCs since 1996 (Fig. 13c). The spatial
 671 patterns and heterogeneous correlation patterns of the summer SVD–
 672 BWTa resemble those of winter one except a little higher correlation
 673 core in summer one.

674 5.2.2.2. SATa. Summer SVD–SATa presents strong signals in the land like
 675 the winter one, but the strong winter zonal signal spanning from the
 676 Asian continent to the eastern North Pacific is not detected (Fig. 14a).
 677 A wave-like signal is found around 60–70°N, a positive–negative
 678 –positive chain from the west to the east. This wave-like signal is seen
 679 in the second and third modes of EOF–SATa. Small cores in the Asian
 680 continent are related to local geographic characteristics, such as deserts,
 681 plateaus, and mountains. The correlation pattern resembles the spatial
 682 pattern of SVD–SATa. Colder SATa in Siberia, Mongolia, northern and
 683 southeastern China is correlated with warmer BWTa, but warmer SATa
 684 in Himalayas and northwestern China is correlated with warmer BWTa
 685 (Fig. 14b). The tropical to subtropical western North Pacific is negatively
 686 correlated with YS in both seasons: we will discuss this correlation in the
 687 section of summer SVD–SSTa. In both winter and summer, temporal
 688 variability is strong in the 1970s and the late 1990s through in the 2000s,
 689 but rather weak in the 1980s through the mid-1990s (Fig. 14c). The
 690 spatial patterns and heterogeneous correlation patterns of the summer
 691 SVD–BWTa is more similar with the first mode EOF–BWTa than those of
 692 the winter SVD–BWTa.

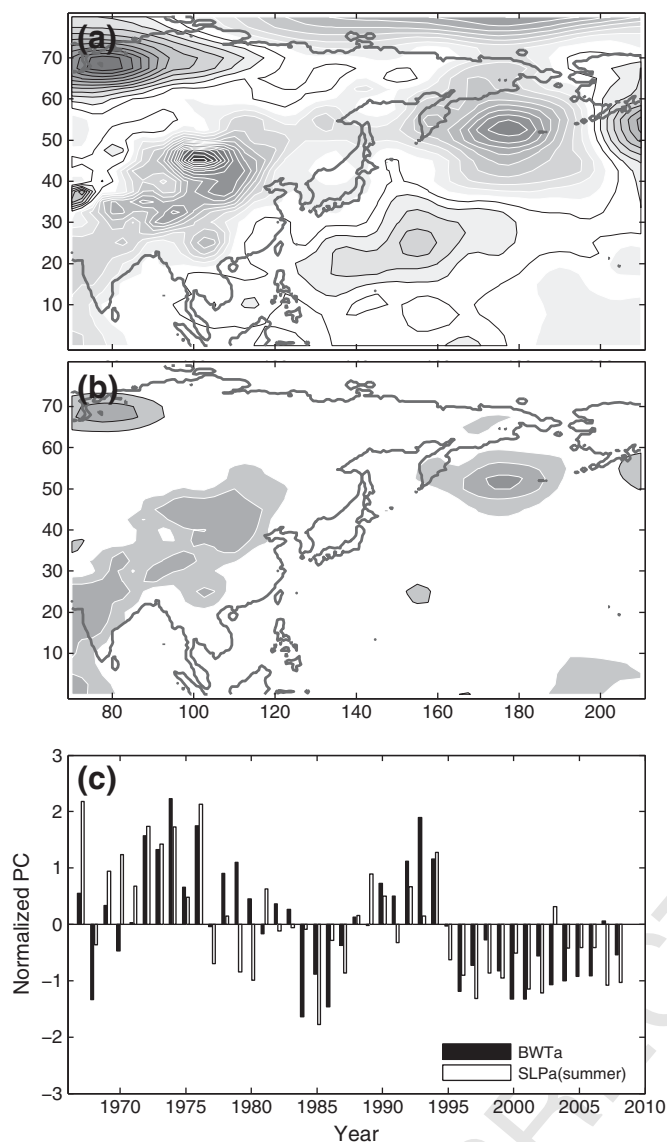


Fig. 13. The first SVD mode of summer SLPa–August BWTa: (a) spatial pattern of SVD–SLPa (negative (positive) white (black)-contoured; contour interval 0.25 hPa), (b) heterogeneous correlation coefficient pattern of SVD–SLPa (negative (positive) white (black)-contoured; contour interval 0.1; coefficient ≥ 0.2 is shaded), (c) temporal pattern of two SVD–PCs normalized by each PCs' standard deviation.

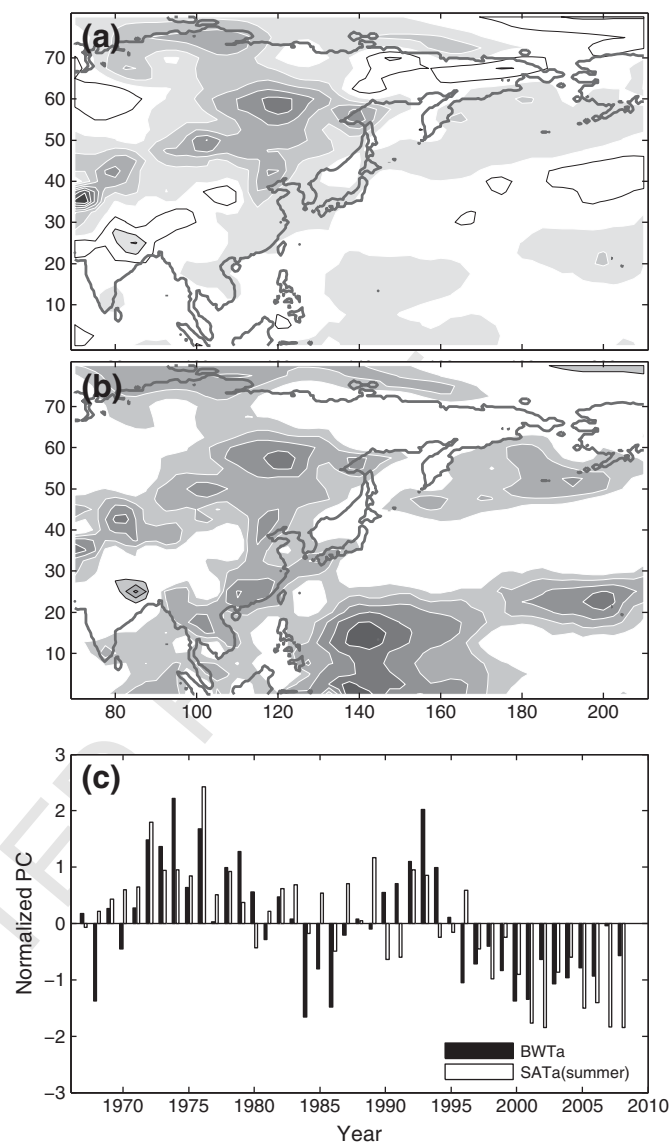


Fig. 14. The first SVD mode of summer SATa–August BWTa. Figure configurations are same as Fig. 13.

693 5.2.2.3. *SSTa*. Summer SVD–SSTa displays a strong zonal band north of
 694 30°N (Fig. 15a). One core is found in the East/Japan Sea, the Yellow Sea,
 695 the East China Sea, and east off Japan, and the other from the Gulf of
 696 Alaska to south of the Bering Sea, which is weaker. The two cores seem
 697 to be involved with two major warm currents in the extratropical North
 698 Pacific, i.e. the Kuroshio and the Alaskan Current—the Alaskan Stream.
 699 They are negatively correlated with BWTa (Fig. 15b): the negative
 700 correlation in the southern YS and the East China Sea (≤ 0.4) was
 701 expected in Section 4.2. The summer SSTa in the central to eastern
 702 tropics indicating occurrences of El Niño seems unlikely to affect BWTa
 703 concurrently, according to a very weak correlation there and the low
 704 correlation with the summer MEI at zero lag (Fig. 9b). The winter SSTa in
 705 the central to eastern tropics affects BWTa moderately.

706 By contrast, the tropical to subtropical western North Pacific SSTa,
 707 also SATa, is strongly correlated to BWTa in both seasons. According to
 708 the estimation from the global SST and SAT datasets used in this study,
 709 the tropical to subtropical western North Pacific shows weaker
 710 variability in SSTa (< 0.5 °C) than the central and eastern tropics, the

Polar Front, the west and east coasts of North Pacific (> 1 °C). So does
 711 it in SATa. However, this variability is considerable in comparison
 712 with an annual cycle amplitude (< 1.5 °C on average) in this region. In
 713 addition, recent studies documented that impact of ENSO on the
 714 climate of East Asia is moderate, compared to other regions (Lau et al.,
 715 2000; Yang et al., 2002). The way that the tropical to subtropical
 716 western North Pacific affects BWTa is different in both seasons. 717

In summer, warming (cooling) in the tropical to subtropical western
 718 North Pacific causes high (low) geopotential height anomalies over East
 719 Asia and the adjacent seas, accompanied by dry and hot conditions there
 720 (Nitta, 1987; Yoo et al., 2004). Thus, warmer SST in YS intensifies the
 721 vertical temperature gradient of the thermocline and induces cold
 722 anomaly in YSCWM by less downward heat transfer through the
 723 thermocline than the normal years (see details in Section 4.2). In winter,
 724 warming (cooling) in the tropical to subtropical western North Pacific is
 725 accompanied by strong (weak) East Asian Jet Stream through a strong
 726 (weak) meridional gradient of the western North Pacific SST. The strong
 727 winter jet stream is associated with strong surface westerlies because of
 728 the barotropicity of the jet stream. The strong surface westerlies, in turn,
 729 increase heat loss from the sea surface by mixing and evaporation 730

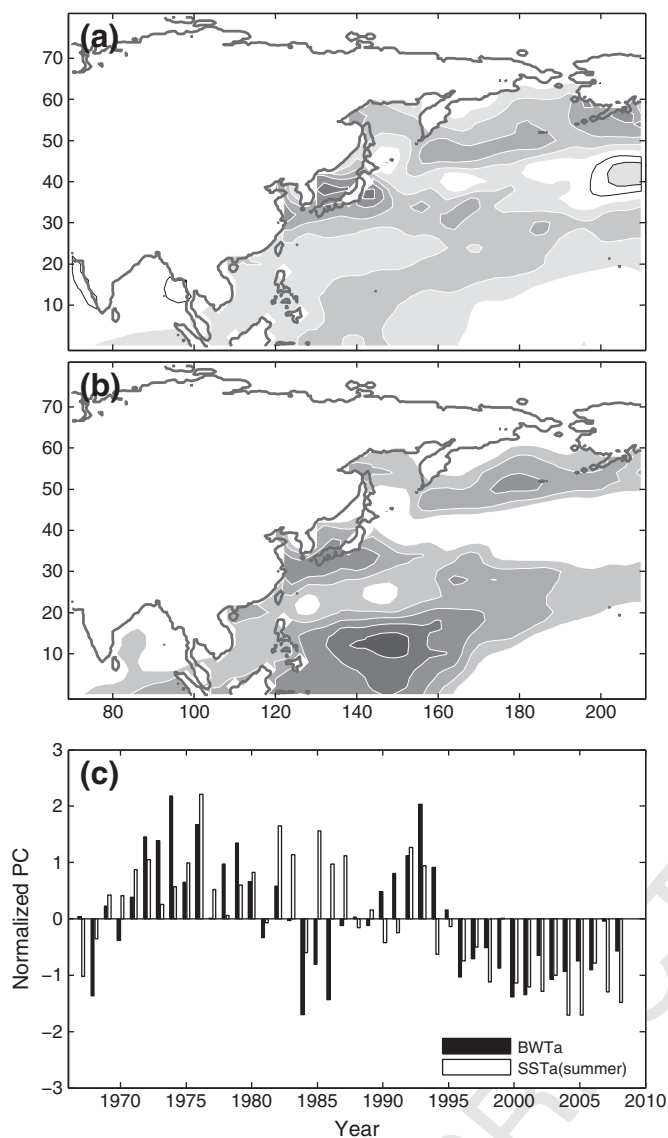


Fig. 15. The first SVD mode of summer SSTA–August BWTa. Figure configurations are same as Fig. 13.

and decrease SST under the westerlies (Yang et al., 2002). This winter colder SST eventually remains as a cold anomaly in YSCWM. In those mechanisms, the tropical to subtropical western North Pacific SSTA is negatively correlated with BWTa in both seasons.

The two PCs are correlated at 0.55. Note that all summer PCs of the background variables are much highly correlated to PC–BWTa after 1996, convincing that the summer forcing plays an important role on cooling YSCWM after 1996 (Fig. 15c). The spatial patterns and heterogeneous correlation patterns of the summer SVD–BWTa resemble those of winter one except a little lower correlation core in winter one.

6. Conclusions

- (1) We identified the characteristics of interannual-to-interdecadal variability of the Yellow Sea Bottom Cold Water Mass (YSCWM) and examined the causes of the variability focusing on seasonally differential forcings. The Korea Oceanographic Data Center dataset was used, which is composed of bimonthly observations over 42 years of 1967–2008.
- (2) The first EOF mode accounting for 53% of the bottom water temperature anomaly (BWTa) variability shows the warming

or cooling over the entire domain with the highest amplitude in the flank of Yellow Sea trough. A dominant period is 2–7 years and 10–20 years. YSCWM reveals three cold events (1967–1971, 1983–1988 and 1996–2008 (i.e. until data is available; there is a pause in 2005)) and two warm events (1972–1980 and 1990–1995) with amplitude larger than 2 °C.

- (3) According to composite maps of those events, a relationship was found between upper and bottom layers in summer: warm (cold) anomaly appears in the upper (bottom) layer in June/August during the cold (warm) events. In the cold events, as the increased vertical temperature gradient of the thermocline impedes the downward heat transfer, the warming of YSCWM which peaks from June to August slows down in comparison with the normal years. In the warm events an opposite scenario occurs.
- (4) During most of the events the bottom layer retains the anomaly induced from the previous winter surface, which is already known, although the bottom layer anomaly strengthens in summer or disappears temporarily for two or four months. The temporal disappearance is probably due to the basin-wide seasonal circulation.
- (5) In the cold event after 1996, on the contrary, the anomaly with the opposite sign to the winter surface anomaly emerges in the bottom layer and matures over the event extending upward: the anomaly in the bottom layer is induced by the summer surface forcing. The summer surface forcing is capable of not only intensifying the anomaly induced in winter but also triggering a new anomaly in the bottom layer, not originated from winter.
- (6) The background atmospheric and oceanic variables affecting August BWTa are seasonally different, according to the correlation analysis on the winter/summer climate indices and the SVD analysis on the winter/summer background variables fields (SLPa, SATa, and SSTA). In winter, strengthening of both the Siberian High and the Aleutian Low causes the cold event in YSCWM. The relation to the Aleutian Low is confirmed by the significant correlation to the North Pacific Index and the Pacific Decadal Oscillation Index. The two indices also lead the YSCWM variability by 2–3 years. The intensified low pressure and cold SATa in the Arctic is also associated with the cold event, supported by the correlation to the Arctic Oscillation Index. The cold SATa featuring the zonal band covering 30–50°N, which agrees with the position of the East Asian Jet Stream, triggers the cold event. The spatial patterns of SVD of SSTA reflect a relation to the Pacific Decadal Oscillation.
- (7) In summer, the Western Pacific Pattern Index is concurrently correlated to BWTa, implying that weakening of the East Asian summer monsoon relates to the warm BWTa. Decreasing SLP in the Asian continent and the Aleutian Islands also results in warmer YSCWM, but the summer SLPa impact is not as dominant as the winter one. SSTA in the Kuroshio and the Alaskan Current—the Alaskan Stream is negatively correlated to BWTa. All summer time-series of principal components of the background variables are much highly correlated to that of BWTa after 1996 than the other period, convincing that the summer forcing plays an important role on cooling YSCWM after 1996.
- (8) SATa/SSTA in the tropical to subtropical western North Pacific is strongly (negative) correlated (≤ 0.5) to BWTa in the both seasons; however, the mechanisms are different between summer and winter. In summer, warming (cooling) in the tropical to subtropical western North Pacific causes high (low) geopotential height anomalies over the East Asia and the adjacent seas, accompanied by dry and hot conditions there (Nitta, 1987; Yoo et al., 2004). Thus warmer SSTA in the Yellow Sea intensifies cold anomaly in YSCWM. In winter, warming

(cooling) in the tropical to subtropical western North Pacific generates a strong (weak) meridional gradient of the western North Pacific SST, which intensifies (weakens) the East Asian Jet Stream. The strong winter jet stream associated with strong surface westerlies decreases SST under the westerlies (Yang et al., 2002). This winter colder SST eventually remains as a cold anomaly in YSCWM.

(9) Contrastly, SATa/SSTa in the central to eastern tropical Pacific (where ENSO occurs) is not concurrently correlated to BWTa in summer, and weakly correlated to BWTa in delayed and/or indirect ways. This result consists with recent studies that impact of ENSO on the climate of the East Asia is moderate, compared with other regions.

(10) Since the remnant of the winter Yellow Sea Warm Current Water remains in the Yellow Sea trough (Lie et al., 2001), YSCWM can be influenced by variability of the Yellow Sea Warm Current. Taking the Pacific Decadal Oscillation into account, the Yellow Sea Warm Current might be the last pathway that the Pacific Decadal Oscillation is transferred through the Kuroshio to the Yellow Sea. It seems much plausible, according to the study of satellite altimeter data supporting that the Kuroshio delivers Pacific Decadal Oscillation through the Tsushima Current, which branches from the Kuroshio, to the Japan/East Sea (Gordon and Giulivi, 2004) and the Tsushima Current feeds the Yellow Sea Warm Current. Unfortunately, the KODC data do not cover the region of the Yellow Sea Warm Current and the East China Sea shelf; a numerical experiment should be followed to testify that hypothesis. In addition, we did not examine the dynamic processes to confirm the suggested mechanisms for the warm and cold events, which remain to be studied.

Acknowledgments

This research was sponsored by the Naval Oceanographic Office, Office of Naval Research, and Naval Postgraduate School. We greatly thank Dr. S. W. Yeh (Korea Ocean Research & Development Institute, Korea) for insightful comments on the manuscript.

References

- Bai, H., Hu, D., Chen, Y., Wang, Q., 2004. Statistic characteristics of thermal structure in the southern Yellow Sea in summer. *Chinese J. Oceanol. Limnol.* 22 (3), 237–243.
- Barnston, A.G., Livezey, R.E., 1987. Classification, seasonality and persistence of low-frequency atmospheric circulation patterns. *Mon. Wea. Rev.* 115, 1083–1126.
- Beckers, J.M., Rixen, M., 2003. EOF calculations and data filling from incomplete oceanographic datasets. *J. Atmos. Ocean. Technol.* 20, 1839–1856.
- Björnsson, H., Venegas, S.A., 1997. A manual for EOF and SVD analyses of climatic data, CCGCR Rep. 97-1. McGill University, Canada.
- Cherry, S., 1996. Singular value decomposition analysis and canonical correlation analysis. *J. Climate* 9, 2003–2009.
- Cherry, S., 1997. Some comments on singular value decomposition analysis. *J. Climate* 10, 1759–1761.
- Cho, K.-D., 1982. On the influence of the Yellow Sea Bottom Cold Water on the demersal fishing grounds. *Bull. Korean. Fish. Tech. Soc.* 18 (1), 25–33.
- Chu, P.C., Chen, Y.C., Kuminaka, A., 2005. Seasonal variability of the East China/Yellow Sea surface buoyancy flux and thermohaline structure. *Adv. Atmos. Sci.* 22, 1–20.
- Chu, P.C., Fralick, C.R., Haeger, S.D., Carron, M.J., 1997a. A parametric model for Yellow Sea thermal variability. *J. Geophys. Res.* 102 (C5), 10499–10508.
- Chu, P.C., Wells, S.K., Haeger, S.D., Szczechowski, C., Carron, M., 1997b. Temporal and spatial scales of the Yellow Sea thermal variability. *J. Geophys. Res.* 102 (C3), 5655–5668.
- Deser, C., Alexander, M.A., Timlin, M.S., 1996. Upper ocean thermal variations in the North Pacific during 1970–1991. *J. Climate* 9, 1840–1855.
- Deser, C., Alexander, M.A., Timlin, M.S., 1999. Evidence for a wind-driven intensification of the Kuroshio Current extension from the 1970s to the 1980s. *J. Climate* 12, 1697–1706.
- Gong, D.-Y., Ho, C.-H., 2003. Arctic Oscillation signals in the East Asian summer monsoon. *J. Geophys. Res.* 108 (D2), 4066. doi:10.1029/2002JD002193.
- Gong, D.-Y., Wang, S.-W., Zhu, J.-H., 2001. East Asian winter monsoon and Arctic Oscillation. *Geophys. Res. Lett.* 28 (10), 2073–2076.
- Gordon, A.L., Giulivi, C.F., 2004. Pacific decadal oscillation and sea level in the Japan/East Sea. *Deep Sea Res. I* 51, 653–663.

- Han, G., Huang, W., 2008. Pacific Decadal Oscillation and sea level variability in the Bohai, Yellow, and East China Seas. *J. Phys. Oceanogr.* 38, 2772–2783.
- Han, Y.H., Chang, S.-D., 1978. Relation between heat budget and the cold water in the Yellow Sea in winter. *Bull. Korean. Fish. Tech. Soc.* 14 (1), 1–14.
- Hong, C.-H., Cho, K.-D., Kim, H.-J., 2001. The relationship between ENSO events and sea surface temperature in the East (Japan) Sea. *Prog. Oceanogr.* 49 (1), 21–40.
- Hu, D., Wang, Q., 2004. Interannual variability of the southern Yellow Sea Cold Water Mass. *Chinese J. Oceanol. Limnol.* 22 (3), 231–236.
- Hur, H.B., Jacobs, G.A., Teague, W.J., 1999. Monthly variations of water masses in the Yellow and East China Seas. *J. Oceanogr.* 55 (2), 171–184.
- Isobe, A., 1999. The Taiwan–Tsushima Warm Current system: its path and the transformation of the water mass in the East China Sea. *J. Oceanogr.* 55 (2), 185–195.
- Kang, Y.Q., Kim, H.-K., 1987. Relationships between the winter-time surface water temperature and the summer-time bottom water temperature in the West Sea of Korea. *J. Oceanol. Soc. Korea* 22 (4), 228–235.
- Lau, K.-M., Kim, K.-M., Yang, S., 2000. Dynamical and boundary forcing characteristics of regional components of the Asian summer monsoon. *J. Climate* 13, 2461–2482.
- Lee, S.-H., Beardsley, R.C., 1999. Influence of stratification on residual tidal currents in the Yellow Sea. *J. Geophys. Res.* 104 (C7), 15679–15701.
- Lie, H.-J., 1986. Summertime hydrographic features in the southeastern Hwanghae. *Prog. Oceanogr.* 17229–17242.
- Lie, H.-J., 1989. Tidal fronts in the southeastern Hwanghae (Yellow Sea). *Cont. Shelf Res.* 9 (6), 527–546.
- Lie, H.-J., Cho, C.-H., Lee, J.-H., Lee, S., Tang, Y., 2000. Seasonal variation of the Cheju Warm Current in the northern East China Sea. *J. Oceanogr.* 56 (2), 197–211.
- Lie, H.-J., Cho, C.-H., Lee, J.-H., Lee, S., Tang, Y., Zou, E., 2001. Does the Yellow Sea Warm Current really exist as a persistent mean flow? *J. Geophys. Res.* 106 (C10), 22199–22210.
- Lin, H., Derome, J., Greatbatch, R.J., Peterson, K.A., Lu, J., 2002. Tropical links of the Arctic Oscillation. *Geophys. Res. Lett.* 29 (20), 1943. doi:10.1029/2002GL015822.
- Mantua, N.J., Hare, S.R., Zhang, Y., Wallace, J.M., Francis, R.C., 1997. A Pacific interdecadal climate oscillation with impacts on salmon production. *Bull. Amer. Meteor. Soc.* 78, 1069–1079.
- McPhaden, M.J., 2002. TAO/TRITON tracks Pacific Ocean warming in early 2002. *CLIVAR Exchanges* 24, pp. 7–9.
- Minobe, S., 2002. Interannual to interdecadal changes in the Bering Sea and concurrent 1998/1999 changes over the North Pacific. *Prog. Oceanogr.* 55, 45–65.
- Minobe, S., Sako, A., Nakamura, M., 2004. Interannual to interdecadal variability in the Japan Sea based on a new gridded upper water temperature dataset. *J. Phys. Oceanogr.* 34, 2382–2397.
- Naimie, C.E., Blain, C.A., Lynch, D.R., 2001. Seasonal mean circulation in the Yellow Sea—a model-generated climatology. *Cont. Shelf Res.* 21, 667–695.
- Nitta, T., 1987. Convective activities in the tropical western Pacific and their impact on the Northern Hemisphere summer circulation. *J. Meteor. Soc. Japan* 65, 373–390.
- Oelke, C., Zhang, T., Serreze, M.C., 2004. Modeling evidence for recent warming of the Arctic soil thermal regime. *Geophys. Res. Lett.* 31 (7), L07208. doi:10.1029/2003GL019300.
- Park, S., Chu, P.C., 2006a. Interannual SST variability in the Japan/East Sea and relationship with environmental variables. *J. Oceanogr.* 62 (2), 115–132.
- Park, S., Chu, P.C., 2006b. Thermal and haline fronts in the Yellow/East China Seas: surface and subsurface seasonality comparison. *J. Oceanogr.* 62 (5), 617–638.
- Park, W.-S., Oh, I.-S., 2000. Interannual and interdecadal variations of sea surface temperature in the East Asian Marginal Sea. *Prog. Oceanogr.* 47, 191–204.
- Park, Y.H., 1986. Water characteristics and movements of the Yellow Sea Warm Current in summer. *Prog. Oceanogr.* 17, 243–254.
- Ponomarev, V., Trusenkova, O., Trousenkov, S., Kaplunenko, D., Ustinova, E., Polyakova, A., 1999. The ENSO Signal in the Northwest Pacific. *Proceedings of The 1998 Science Board Symposium on The Impacts of the 1997/98 El Niño Event on the North Pacific Ocean and Its Marginal Seas*. Pacific Oceanological Institute Russian Academy of Sciences, pp. 13–30.
- Stephens, C., Levitus, S., Antonov, J., Boyer, T.P., 2001. On the Pacific Ocean regime shift. *Geophys. Res. Lett.* 28 (19), 3721–3724.
- Su, Y.-S., Weng, X.-C., 1994. Water masses in China Seas. In: Zhou, D., Liang, Y.-B., Tseng, C.K. (Eds.), *Oceanology of China Seas*, vol.1. Kluwer Academic Publishers, The Netherlands, pp. 3–16.
- Teng, S.K., Yu, H., Tang, Y., Tong, L., Choi, C.I., Kang, D., Liu, H., Chun, Y., Juliano, R.O., Rautalahti-Miettinen, E., Daler, D., 2005. Global international waters assessment: Yellow Sea. *GIWA Regional Assessment*, 34. University of Kalmar, Sweden.
- Thompson, D.W.J., Wallace, J.M., 1998. The Arctic Oscillation signature in the wintertime geopotential height and temperature fields. *Geophys. Res. Lett.* 25 (9), 1297–1300.
- Trenberth, K.E., Hurrell, J.W., 1994. Decadal atmosphere–ocean variations in the Pacific. *Climate Dynamics* 9, 303–319.
- Wang, B., Wu, R., Fu, X.H., 2000. Pacific–East Asian teleconnection: how does ENSO affect East Asian climate? *J. Climate* 13 (9), 1517–1536.
- Wang, R., Zuo, T., 2004. The Yellow Sea Warm Current and the Yellow Sea Cold Bottom Water: their impact on the distribution of zooplankton in the Southern Yellow Sea. *J. Korean Soc. Oceanogr.* 39 (1), 1–13.
- Wang, R., Zuo, T., Wang, K., 2003. The Yellow Sea Cold Bottom Water—an over-summering site for *Calanus sinicus* (Copepoda, Crustacea). *J. Plankton Res.* 25 (2), 169–183.
- Wolter, K., Timlin, M.S., 1993. Monitoring ENSO in COADS with a seasonally adjusted principal component index. *Proc. of the 17th Climate Diagnostics Workshop*. Climate Analysis Center, NOAA, pp. 52–57.
- Wolter, K., Timlin, M.S., 1998. Measuring the strength of ENSO—how does 1997/98 rank? *Weather* 53, 315–324.

- 972 Wu, B., Wang, J., 2002. Winter Arctic Oscillation, Siberian High and East Asian Winter
973 Monsoon. *Geophys. Res. Lett.* 29 (19), 1897. doi:10.1029/2002GL015373.
- 974 Yang, S.-K., Cho, K.-D., Hong, C.-H., 1984. On the abnormal low temperature
975 phenomenon of the Yellow Sea Bottom Cold Water in Summer 1981. *J. Oceanol.
976 Soc. Korea* 19 (2), 125–132.
- 977 Yang, S., Lau, K.-M., Kim, K.-M., 2002. Variations of the East Asian Jet Stream and Asian-
978 Pacific-American winter climate anomalies. *J. Climate* 15 (3), 306–325.
- 986
- Yoo, S.-H., Ho, C.-H., Yang, S., Choi, H.-J., Jhun, J.-G., 2004. Influences of tropical-western
979 and extratropical Pacific sea surface temperatures on the east and Southeast Asian
980 climate in the summers of 1993–94. *J. Climate* 17 (13), 2673–2687. 981
- Zhang, S.W., Wang, Q.Y., Lu, Y., Cui, H., Yuan, Y.L., 2008. Observation of the seasonal evolution
982 of the Yellow Sea Cold Water Mass in 1996–1998. *Cont. Shelf Res.* 28, 442–457. 983
- Zhang, Y., Wallace, J.M., Battisti, D.S., 1997. ENSO-like interdecadal variability: 1900–93. 984
985 *J. Climate* 10, 1004–1020.

UNCORRECTED PROOF